



저작자표시-비영리-변경금지 2.0 대한민국

이용자는 아래의 조건을 따르는 경우에 한하여 자유롭게

- 이 저작물을 복제, 배포, 전송, 전시, 공연 및 방송할 수 있습니다.

다음과 같은 조건을 따라야 합니다:



저작자표시. 귀하는 원 저작자를 표시하여야 합니다.



비영리. 귀하는 이 저작물을 영리 목적으로 이용할 수 없습니다.



변경금지. 귀하는 이 저작물을 개작, 변형 또는 가공할 수 없습니다.

- 귀하는, 이 저작물의 재이용이나 배포의 경우, 이 저작물에 적용된 이용허락조건을 명확하게 나타내어야 합니다.
- 저작권자로부터 별도의 허가를 받으면 이러한 조건들은 적용되지 않습니다.

저작권법에 따른 이용자의 권리와 책임은 위의 내용에 의하여 영향을 받지 않습니다.

이것은 [이용허락규약\(Legal Code\)](#)을 이해하기 쉽게 요약한 것입니다.

[Disclaimer](#)



공학박사 학위논문

**Designing Transparent Electrodes Materials
Toward Broadband Light Trapping**

광대역 광포획을 위한 투명 전극 물질 개발

2015년 8월

서울대학교 대학원
재료공학부
이우진

Designing Transparent Electrodes Materials

Toward Broadband Light Trapping

광대역 광포획을 위한 투명 전극 물질 개발

지도교수 박 병 우

이 논문을 공학박사 학위논문으로 제출함.

2015년 4월

서울대학교 대학원
재료공학부
이 우 진

이우진의 공학박사 학위논문을 인준함.

2015년 6월

위 원 장	<u>유 상 임</u>	(인)
부위원장	<u>박 병 우</u>	(인)
위 원	<u>남 기 태</u>	(인)
위 원	<u>신 병 하</u>	(인)
위 원	<u>문 태 호</u>	(인)

Abstract

Transparent conducting oxides (TCOs) have been used for various optoelectronic applications, such as flat-panel displays and thin-film solar cells. Especially for *a*-Si thin-films solar cells, light-scattering capability of TCOs via surface texturing is one of the most important characteristics due to effective scattering enhances power-conversion efficiency. Among various TCOs, ZnO:Al has received strong attention because of its larger feature size by wet-chemical etching. Basically, textured morphology by wet etching depends on the nanostructure of TCOs due to the anisotropy of etching rates. However, nanostructural control of TCOs in mass manufacturing is pretty limited with consideration of electrical conductivity and high throughput. Therefore, surface texturing by simple etching for the given TCO nanostructures offers a great merit for the strategy of TCO development.

In this thesis, the novel etching system by organic acid for the surface-textured ZnO:Al films is investigated. The Chap. 1 describes the general scientific context and the research field in which this thesis is included. First, a brief overview of the photovoltaic technologies and the current issues of the Si thin-film solar cells. Second, the TCOs are introduced and their use as a front electrode in Si thin-film solar cells is explained. Finally, the motivation and objectives of this work are summarized.

In Chap. 2, an organic acid for the surface texturing of ZnO:Al is introduced as an alternative to conventional HCl. The texturing behavior by oxalic acid is investigated in terms of vertical roughness, lateral correlation length, and thickness change according to the crater evolution. Etching with oxalic acid results in superior light-scattering performance (by ~8% increase at $\lambda = 1000$ nm) with maintaining transparency and resistance, compared to etching with HCl. This fascinating behavior is understood by crater evolution with the difference in relative etching rates. Significantly, this simple and reproducible texturing tactic extends tunability for desirable TCO morphology, enabling efficient light trapping, and therefore appears potentially applicable for large-scale photovoltaic devices in industry. Lastly, all results and conclusion of the thesis are summarized in Chap. 3.

Keywords: Transparent Conducting Oxides, Al-doped ZnO, Thin-Film Solar Cells, Photovoltaics, Surface Texturing, Light Trapping

Student Number: 2011-31282

Table of Contents

Abstract	i
List of Figures	v
List of Table	xiv
Chapter 1. Overview	1
1.1. General Introduction to Solar Cells	1
1.1.1. Basic Operation Principle of the Solar Cells	1
1.1.2. Classification of Solar Cells	7
1.2. Si Thin Film Solar Cells	11
1.2.1. Introduction of the Si Thin Film Solar Cells	11
1.2.2. Light Management Technology in Si Thin Film Solar Cells	13
1.3. Overview of Transparent Conducting Oxide in Si Thin Film Solar Cells	17
1.3.1. The Factors determining Textured Morphology	21
1.3.2. The Wet-Chemical Etching of ZnO:Al Films	27
1.4. References	39
Chapter 2. Organic-Acid Texturing of ZnO:Al Toward Broadband Light Scattering for Si Thin-Film Solar Cells	44
2.1. Introduction	44
2.2. Experimental Section	46
2.3. Results and Discussion	46
2.4. Conclusions	68
2.5. References	69
Chapter 3. Summary	73

Appendix

A. 1. Facile Conversion Synthesis of Densely-Formed Branched ZnO Nanowire Arrays for Quantum-Dot-Sensitized Solar Cells	74
A.1.1. Introduction	74
A.1.2. Experimental Section	76
A.1.2.1. Synthesis of 1-D Nanostructures	76
A.1.2.2. Branched ZnO Nanowire Growth	77
A.1.2.3. Device Fabrication	77
A.1.2.4. Characterization	78
A.1.3. Results and Discussion	79
A.1.4. Conclusions	101
A.1.5. References	102
A. 2. List of Publications and Presentations	109
A.3.1. Publications (International)	109
A.3.2. Presentation (International)	113
A.3.3. Presentation (Domestic)	113
국문 초록	114

List of Figures

Chapter 1.

Fig. 1-1. (Color) Schematic drawing of photovoltaic process and loss process in $p-n$ junction solar cell: (1) non absorption of below bandgap photons, (2) lattice thermalization loss, (3) junction loss, (4) contact voltage loss, (5) recombination loss. From Ref. [2].

Fig. 1-2. (Color) Photocurrent-voltage characteristics of a typical solar cell in the dark and light illuminated condition.

Fig. 1-3. (Color) The effect of series (a) and parallel resistance (b). The outer curve in each case represents $R_s = 0$ and $R_{sh} = \infty$. From Ref. [3].

Fig. 1-4. (Color) Solar cells classification: silicon type, compound semiconductor type, and organics.

Fig. 1-5. (Color) Best research-cell efficiency from National Renewable Energy Laboratory (NREL). From Ref. [5]

Fig. 1-6. (Color) Current issues in development of triple-junction Si thin film solar cells.

Fig. 1-7. (Color) Schematic sketch of the cross section of a Si thin-film solar cell. The arrows representing incoming and scattered light. From Ref. [15].

Fig. 1-8. (Color) Optical losses by non-absorber layer in Si thin film solar cells. From Ref. [16].

Fig. 1-9. (Color) Absorption coefficient of the different absorber layers in solar cells. Ref. [17]

Fig. 1-10. (Color) (a) Absorbance of a smooth (solid line) and textured ZnO layer (dashed line) as a function of wavelength. From Ref. [15] (b) Quantum efficiency of two identically deposited *p-i-n* cells on smooth and etch-textured ZnO. From Ref. [18].

Fig. 1-11. (Color) The modified Thornton model showing the correlation between deposition parameters, structural film properties, and etching behaviour of sputtered ZnO:Al films on glass substrates. From Ref. [20].

Fig. 1-12. (Color) Schematic illustrations of etching behavior types in a matrix of parameter substrate temperatures and TAC (target Al concentration).

From Ref. [21].

Fig. 1-13. (Color) Residual stress of ZnO:Al films as a function of (a) Al contents and (b) substrate temperature. From Ref. [22] and [23].

Fig. 1-14. (Color) SEM images of textured Morphology for ZnO:Al films by various etching agents. (a) Etching by 0.1 M HCl for 40 s, (b) by 0.5 M NH₄Cl for 270 s, (c) by 0.3 M HF for 70 s, and (d) by 0.5 M KOH, respectively. From Ref. [23-25].

Fig. 1-15. (Color) Schematic illustration of (a) ZnO wurtzite structure and (b) dangling bond model for etching of a ZnO single crystal. Dotted lines are either projection lines or correspond to bonds that are hidden behind atoms. From Ref. [26].

Fig. 1-16. (Color) Schematic illustrations of etching model describing three postulates. a) planar (left) and cross-sectional (right) views of the different etching potentials of the grain boundaries for a ZnO film. (b) interaction of the etchants with the ZnO film depending on the etchant size: large (left) and small etchant (right), at different etching potentials. (c) resulting crater morphologies with vertically (left) and laterally (right) limited etching rates. Ref. [27]

Fig. 1-17. (Color) A proposed structures of water-hydrionium complex, $\text{H}(\text{H}_2\text{O})_n^+$, produced when an acid ionizes in water. In case of the value of n in $\text{H}(\text{H}_2\text{O})_n^+$ is 6. From Ref. [32].

Fig. 1-18. (Color) Schematic representations of etching progress with a period of etching time for oxalic and formic acids. From Ref. [34].

Fig. 1-19. (Color) Schematic illustrations of Diagrams of an etching model to illustrate the etching process. The etching reaction and product diffusion co-dominate the process to form crater-like structures. Ref. [28]

Chapter 2.

Fig. 2-1. (Color) SEM images of the ZnO:Al thin films textured by (a) HCl and (b) oxalic acid.

Fig. 2-2. (Color) (a) AFM image of a ZnO:Al thin film textured by oxalic acid. (b) Sectioned surface profile from the AFM image. (c) Normalized autocorrelation function from the surface profile.

Fig. 2-3. (Color) Extraction of vertical roughness (σ_{rms}) and lateral correlation length (a_{corr}) from AFM data. Etching time dependency by HCl (a-c). For each panel, AFM image (left), 2-D contour plot of autocorrelation function (center), and the autocorrelation function averaged over the azimuth angle ($\tau^2 = \tau_x^2 + \tau_y^2$), with the Gaussian fitting (right).

Fig. 2-4. (Color) Extraction of vertical roughness (σ_{rms}) and lateral correlation length (a_{corr}) from AFM data. Etching time dependency by oxalic acid (a-c). For each panel, AFM image (left), 2-D contour plot of autocorrelation function (center), and the autocorrelation function averaged over the azimuth angle ($\tau^2 = \tau_x^2 + \tau_y^2$), with the Gaussian

fitting (right).

Fig. 2-5. (Color) Cross-sectional AFM images of the textured ZnO:Al films.
(a-c) Etching-time dependence by HCl. (d-f) Etching-time dependence by oxalic acid.

Fig. 2-6. (Color) Optical and electrical properties for the textured ZnO:Al films.
(a-b) Total transmission and haze curves by (a) HCl and (b) oxalic acid.
(c) A plot of haze (at $\lambda = 1000$ nm) vs. sheet resistance.

Fig. 2-7. (Color) (a) Haze curves etching by HCl (90 s) and oxalic acid (15 min).
The solid lines are represented the fitting by Eq. (3). (b) Comparison of surface roughness parameters from AFM and haze.

Fig. 2-8. (Color) Haze-contour plot as a function of σ_{rms} and a_{corr} at different wavelengths (from Eq. (3)).

Fig. 2-9. (Color) X-ray diffraction patterns of the ZnO:Al film. The peak intensities and positions from the hexagonal ZnO (JCPDS #36-1451) are shown as solid green bars.

Fig. 2-10. (Color) Cross-sectional SEM images of the textured ZnO:Al films.
(a-c) Etching-time dependence by HCl. (d-f) Etching-time dependence by oxalic acid. Average thickness is denoted for each panel.

Fig. 2-11. (Color) Etching evolution mechanisms. Schematic illustrations of the phenomenological model, showing the vertical etching through grain boundaries at the initial etching stage (top), and the resultant crater morphologies determined by the competition between vertical etching through the high-angle grain boundaries and lateral etching into the grains (bottom). In case of the oxalic acid, mass transport into grain boundaries is relatively limited due to the larger size of reactants, slowing down the vertical-etching speed compared to that of the lateral etching, which in turn induces larger crater formation at the given etching depth.

Fig. 2-12. (Color) Schematic illustrations showing light-trapping effects by surface texturing of the front TCOs in Si thin-film solar cells. ZnO:Al textured by (a) HCl and (b) oxalic acid. Relative intensities and wavelengths for scattered lights are represented while the scattering angle is arbitrarily shown.

Appendix 1.

Fig. A1-1. (Color) Schematic illustration of the nanostructural evolution in 3-dimensional hierarchical ZnO nanowires with various treatments

Fig. A1-2. (Color) Cross-sectional SEM of densely-formed branches ZnO nanowire arrays with various TAA (thioacetamide) treatments: (a) No treatment (bare), (b) 1-h, (c) 6-h, and (d) 24-h TAA treatments.

Fig. A1-3. (Color) Optical properties of hierarchical ZnO nanostructures at various TAA treatment times: (a) Absorptance and diffused reflectance spectra before CdS sensitization. (b) Diffused transmittance spectra after CdS sensitization.

Fig. A1-4. (Color) Typical SEM and TEM images of ZnO nanostructures during each synthesis procedure (with 6-h TAA treatment time): (a) Bare, (b) ZnO/ZnS core/shell nanowires, (c) ZnO/ZnO core/nanoparticle nanowires, and (d) Branched ZnO.

Fig. A1-5. (Color) X-ray diffraction of the nanostructures showing the crystalline-phase evolution.

Fig. A1-6. (Color) X-ray diffraction of 3-D branched ZnO nanostructures with

various TAA treatment times (after oxidation of ZnS shell and hydrothermal growth of ZnO branches).

Fig. A1-7. (Color) Grain size of ZnO along the $[hkl]$ directions as a function of TAA treatment time.

Fig. A1-8. (Color) Photocurrent-voltage curves of the QDSCs based on the nanostructured photoanodes with different TAA treatment times.

Fig. A1-9. (Color) Incident photon-to-current conversion efficiency (IPCE) spectra.

Fig. A1-10. (Color) Electrochemical impedance spectra of Nyquist plot for the QDSCs (6 h of TAA treatment time) with and without TiO₂ treatment. The inset exhibits the Bode plots. Solid lines are the fitting results using the equivalent circuit model in the inset.

Fig. A1-11. (Color) Experimental decay curves of V_{oc} for the QDSCs. The inset shows the corresponding electron lifetimes.

Fig. A1-12. (Color) Diffused transmittance spectra after the CdS sensitization for the QDSCs (6-h TAA treatment), with and without TiO₂ treatment.

List of Table

Chapter 2.

Table. 2-1. Comparison of the surface parameters obtained from the AFM and haze data.

Table AI. Atomic ratios measured from the ICP results of CdS sensitizers with various TAA treatment times.

Table AII. Photovoltaic performance of the QDSCs. Short-circuit current density (J_{sc}), open-circuit voltage (V_{oc}), fill factor (FF), and power-conversion efficiency (η) of the QDSCs with various TAA treatment times.

Table AIII. Impedance parameters extracted using the equivalent-circuit model for QDSCs.

Chapter 1. Overview

1.1. General Introduction to Solar Cells

1.1.1. Basic operation principle of the Solar Cells

Solar energy is the most promising candidate for renewable energy resources.

The biggest advantage over the conventional power generation systems is that the sunlight can be directly converted into solar energy with the help of solar cells.

This type of electrical energy generation is cost-effective, non-toxic, and follows green approach. The basic operation principle of the solar cells is shown in Fig.

1-1. Each cell consists of two different semiconductor layers i.e. *p*-type material and *n*-type material, and electron-hole pairs will be generated when the incident photon has an energy greater than the band gap of this combination of materials.

In the second step, the generated carriers are separated by the electric field existing at the *p-n* junction, and the final step is the collection of the light-generated carriers flow through the external circuit.

Figure 1-2 shows the photocurrent-voltage characteristics of a typical solar cell in the dark and light illuminated condition. The short-circuit current density (J_{sc}) is the current through the solar cell when voltage across the solar cell is zero. The open-circuit voltage (V_{oc}) is defined as the maximum voltage available from the solar cell and this occurs at zero. The maximum power point (P_{max}) is the

condition under which the solar cell generates its maximum power; the current and voltage in this condition are defined as J_{max} and V_{max} , respectively. The fill factor (FF) and the power conversion efficiency (η) are factors used to characterize the performance of the solar cell. The fill factor is defined as the ratio of P_{max} divided by the product of J_{sc} and V_{oc} . The conversion efficiency is determined as the fraction of incident power which is converted to electricity and is defined as:

$$P_{max} = V_{oc} J_{sc} FF$$

$$\eta = \frac{V_{oc} J_{sc} FF}{P_{in}}$$

The V_{oc} is limited by bandgap energy, cannot exceed E_{gap}/q , and it has lower values than bandgap energy because of the charge recombination. At the V_{oc} , all the photo-carriers recombine within the solar cell diode. In case of the cell with the minimized recombination characteristics, the V_{oc} can be more closely approach the limit value (E_{gap}/q). In ideal case, $p-n$ junction solar cell follows diode characteristics. However, the presence of series resistance and parallel resistance, fill factor exhibits lower value than ideal case. The series resistance comes from transport resistance, contact resistance, and so on. And the parallel (or shunt) resistance is related with unwanted recombination. To achieve highly efficient solar cell, the series resistance must be minimized, and the parallel resistance must be maximized. Figure 1-3 shows effect of the resistance parameter on the $I-V$

characteristics of solar cells.

Figure 1-1 also shows a loss mechanisms that limit the efficiency of in *p-n* junction solar cells. The two most significant loss mechanisms in single bandgap cells are the inability to absorb photons with energy less than the bandgap (process 1), and lattice thermalisation of photon energy exceeding the bandgap (process 2). Shockley and Queisser demonstrated that the one-Sun efficiency limit for a single-material cell is around 31% with an optimal band gap of 1.3 eV [1]. This assumes that the unavoidable losses from the device are the emission of photons produced by radiative recombination, and includes voltage drops across the contacts and junction, denoted by process 3 and 4. Process 5 shows the recombination of electron-hole pairs, and this loss process can be minimized through maintaining long minority carrier lifetimes in the semiconductor materials.

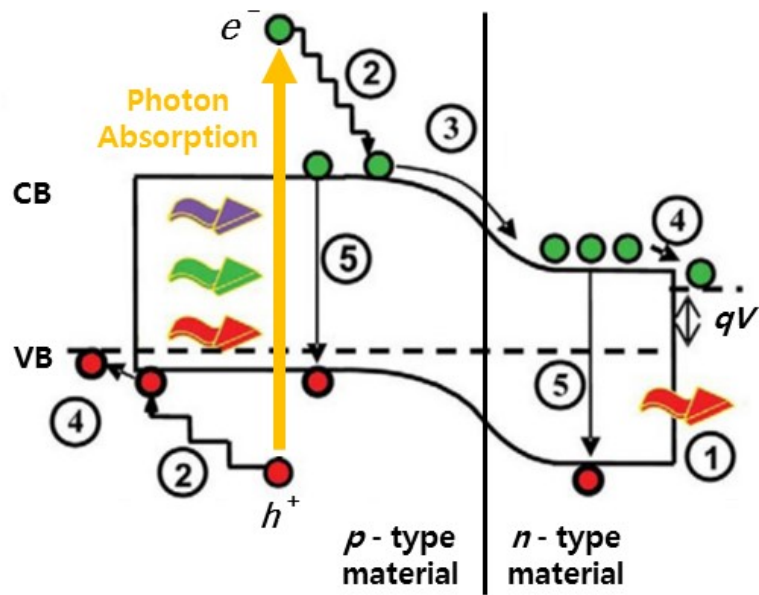


Fig. 1-1. (Color) Schematic drawing of photovoltaic process and loss process in p - n junction solar cell: (1) non absorption of below bandgap photons, (2) lattice thermalization loss, (3) junction loss, (4) contact voltage loss, (5) recombination loss. From Ref. [2].

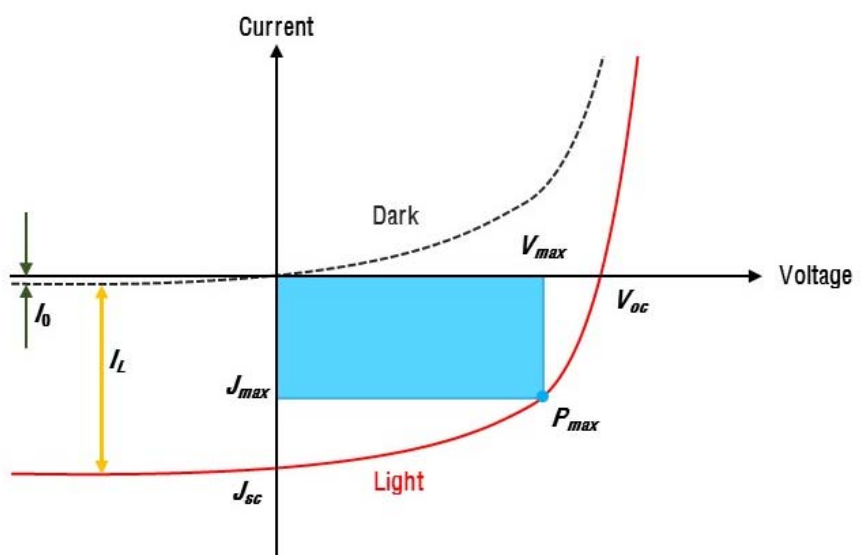
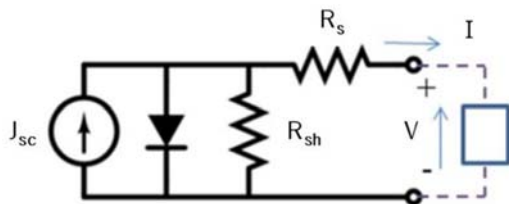
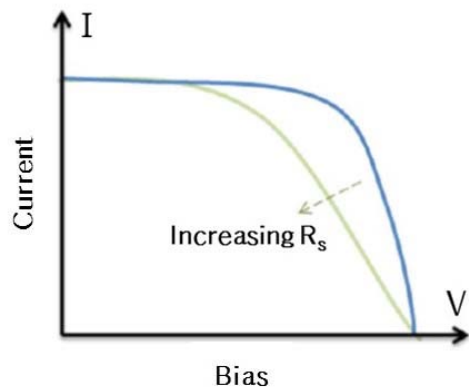


Fig. 1-2. (Color) Photocurrent-voltage characteristics of a typical solar cell in the dark and light illuminated condition.



(a)



(b)

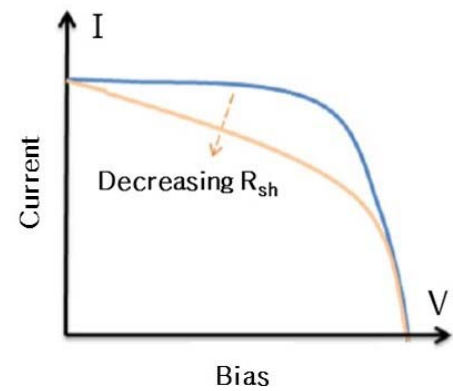


Fig. 1-3. (Color) The effect of series (a) and parallel resistance (b). The outer curve in each case represents $R_s = 0$ and $R_{sh} = \infty$. From Ref. [3].

1.1.2. Classification of Solar Cells

The solar cells could be divided into two parts, organic and non-organic solar cells, by the type of active materials as shown in Fig. 1-4. The organic types have polymer solar cell, dye-sensitized solar cell (DSSCs), and perovskite solar cells which is taking advantages of manufacturing costs and applicability to flexible substrates. However, these types of solar cells show lower power conversion efficiency and compare to other types.

Non-organic types could be classified by silicon and compound semiconductor solar cells. Silicon is one of the most abundant elements in the earth's crust and it has a suitable energy band gap of 1.1 eV for photovoltaic applications. Silicon solar cells are categorized as their crystallinity and also divided into bulk types or thin film types by their thickness. Crystalline silicon is the material most commonly used in the photovoltaic (PV) industry, and wafer-based *c*-Si solar cells and modules dominate the current solar market. Multi-crystalline silicon cells have a more disordered atomic structure that leads to lower efficiencies. However, they are less expensive and more resistant to degradation due to irradiation. Amorphous silicon solar cell is the most developed and widely known for thin-film solar cells. It can be deposited on cheap and very large substrates based on continuous deposition techniques, thus considerably reduce the manufacturing costs. The main disadvantage of this type of solar cells is that they suffer from a

significant reduction in power output over time (35% to 15%), as the sun degrades their performance [4]. A notable variant of amorphous Si thin-film solar cells is the multi-junction thin film silicon (a -Si/ μ -Si) which consist of a -Si cell with additional layer of a -Si and micro-crystalline silicon (μ c-Si) applied onto the substrate. The advantage of the μ c-Si layer is that it absorb more light from the red and near infrared part of the light spectrum, thus increases the efficiency by up to 10%. The thickness of the μ c-Si layer is approximately 3 μ m and makes the cells thicker and more stable.

The other part of thin film solar cell is the compound semiconductor solar cells. CdTe cells are a type of II-VI semiconductor thin film that has a relatively simple production process, which allows the lower production costs. Thus, CdTe the technology has achieved the highest production level of all the thin film technologies. Cu-In-Se (CIS) and Copper-Indium-Gallium-Diselenide (CIGS) cells offer the highest efficiencies of all thin-film PV technologies. Current module efficiencies of compound semiconductor solar cells up to 23.3% have been achieved, close to that of c -Si cells (Fig. 1-5). However, these compound semiconductor materials are toxic and less abundant than silicon.

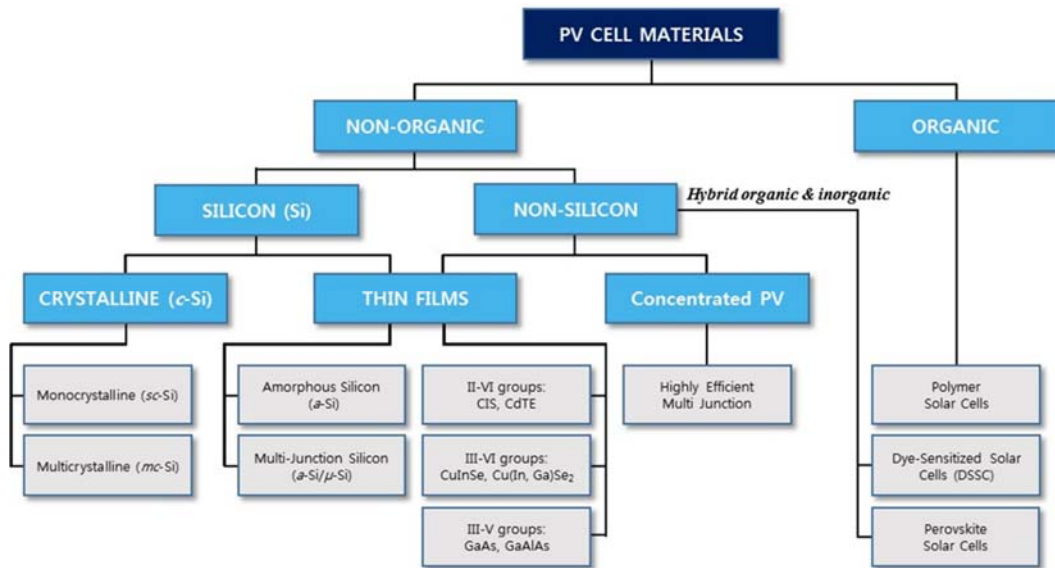


Fig. 1-4. (Color) Solar cells classification: silicon type, compound semiconductor type, and organics.

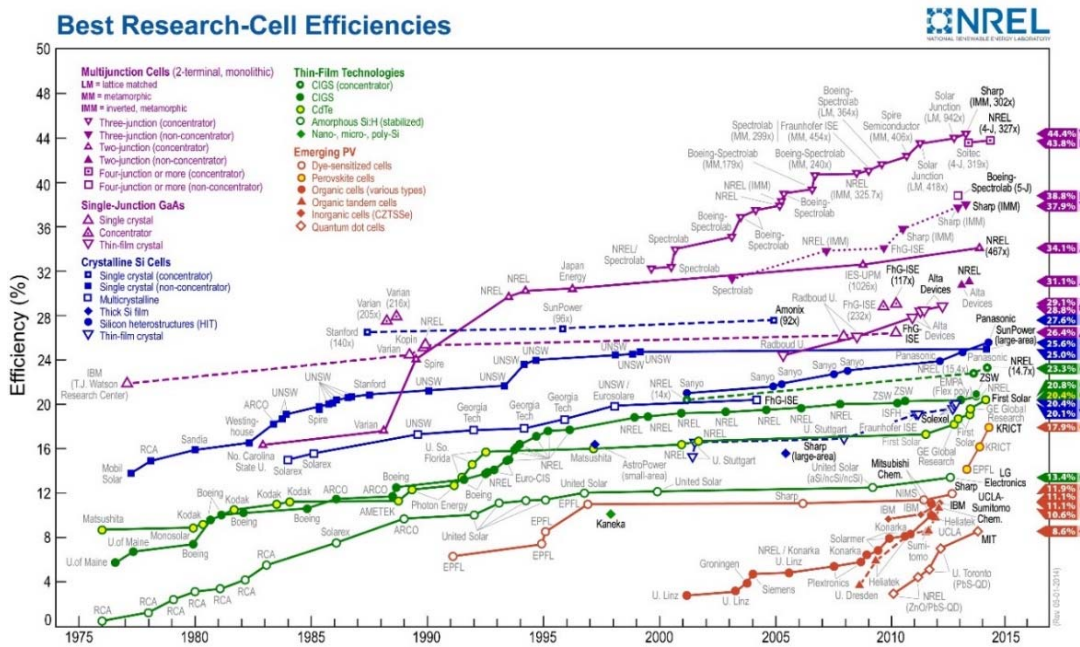


Fig. 1-5. (Color) Best research-cell efficiency from National Renewable Energy Laboratory (NREL). From Ref. [5].

1.2. Si Thin-Film Solar Cells.

1.2.1. Introduction of Si Thin Film Solar Cells.

There are two types of Si thin-film solar cell structures: the amorphous Si (*a*-Si) single-junction structure and the multi-junction (double- and triple-junction). Amorphous Si single-junction solar cells basically are comprised of a glass substrate, a transparent conducting oxide (TCO) layer with a *p-i-n* structure, and a backside reflection layer, and an electrode. The conversion efficiencies of the above *a*-Si solar cells are 9-10% for small-area and large-area single-junction cells, respectively. To apply *a*-Si solar cells to residential PV systems, a higher module conversion efficiency (at least 10%) is required. With the aim of developing high-efficiency devices, the focus of development has been shifting to *a*-Si/*μc*-Si double-junction or *a*-Si/*μc*-Si-based triple-junction solar cells.

Figure 1-6 shows the technological developments necessary to achieve triple-junction solar cells. In order to achieve the goals of both increased conversion efficiency and reduced manufacturing costs simultaneously, material development and performance improvement are required [6-10].

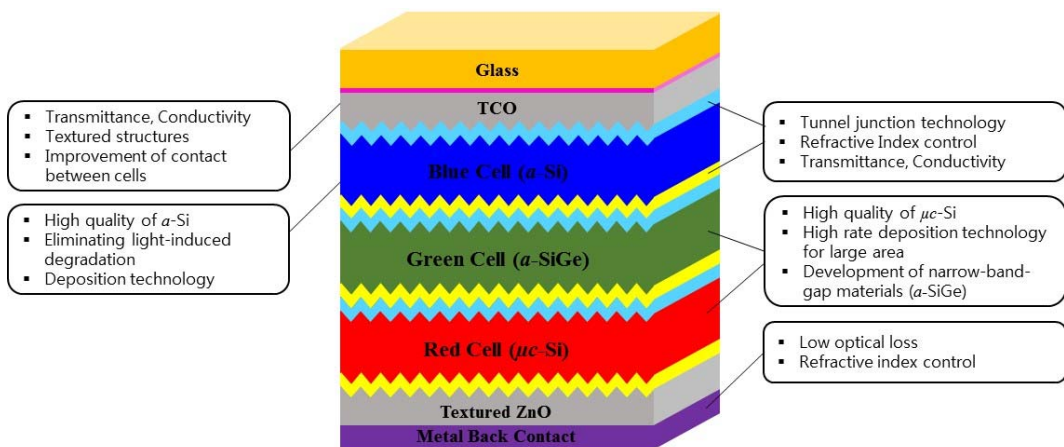


Fig. 1-6. (Color) Current issues in development of triple-junction Si thin film solar cells.

1.2.2. Light Management Technology in Si Thin-Film Solar Cells.

Light management is one of the key issues for improving the performance of Si thin film solar cells and decreasing the production costs by shortening deposition times and using less material. In particular, light management can be divided into two parts; (i) efficient trapping and enhanced absorption of incident light inside absorber layers and (ii) minimization of reflection losses at the front interfaces and absorption losses in the solar cell outside the absorber layers (Fig. 1-7).

For the efficient light utilization, front TCO plays an important role in light trapping by transmitting and scattering light into the absorber layer. TCO layers are required to have a high conductivity of 1×10^4 S/cm and a high transmittance at long wavelengths, and an appropriately textured surface. Low resistivity is necessary to increase the collection efficiency at long-wavelength light. Because the transmittance at long wavelengths depends on the amount of photons absorbed by free carriers, the development of TCO materials with low carrier concentrations and high carrier mobility is desired. Surface texturing is crucial for confining light. However, an excessively textured surface causes cracks to develop from the concave base during the deposition of *a*-Si thin film, decreasing the open voltage and fill factor.

Minimization of reflection and absorption losses outside the absorber layers

relates to the implementation of properly designed anti-reflecting layers and reduction of optical losses in the supporting layers, such as contacts and *p*- and *n*-doped layers in *p-i-n* devices (Fig. 1-8). To decrease optical losses in doped layers a continuous attention is paid to the development the wide band gap doped semiconductors based on *a*-Si:H and *μc*-Si:H such as hydrogenated amorphous/microcrystalline silicon carbide (*a*-SiC:H/*μc*-SiC:H) and hydrogenated amorphous/microcrystalline silicon oxide (*a*-SiO:H/*μc*-SiO:H) [11-13].

In order to suppress the reflection by the TCO/Si interface, anti-reflecting (AR) layer are also incorporated. An effective way to control the AR effect directly is by inserting a transparent material with higher refractive index than SnO₂ or ZnO, such as TiO₂ or Ta₂O₅ [10]. When applying such materials to the TCO/Si interface in thin film Si solar cells, one must consider not only their refractive indices but also their conductivity (i.e., the series resistance of the interface) and durability to reductive plasmas.

For effective light trapping, a highly reflective back contact (BR) is necessary when the average photon is reflected many times at the back side of the solar cell. To satisfy this optical condition together with sufficient electrical conductivity of the back contact, aluminum and silver are commonly used materials as metal back reflectors [14]. Often aluminum is preferred in an industrial module production due to its lower price and better adhesion properties.

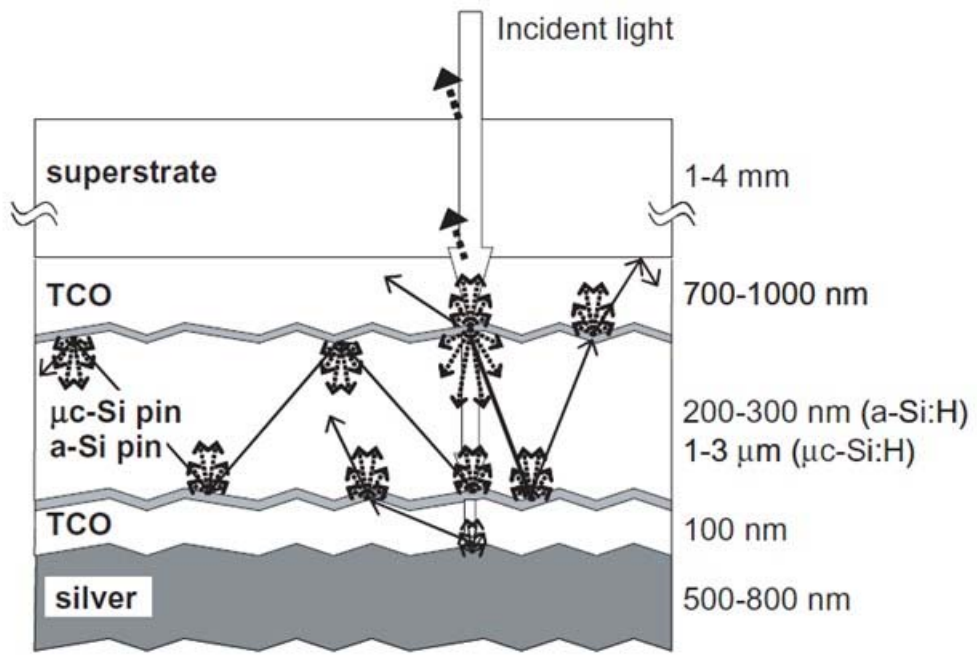


Fig. 1-7. (Color) Schematic sketch of the cross section of a Si thin film solar cell.

The arrows representing incoming and scattered light. From Ref. [15].

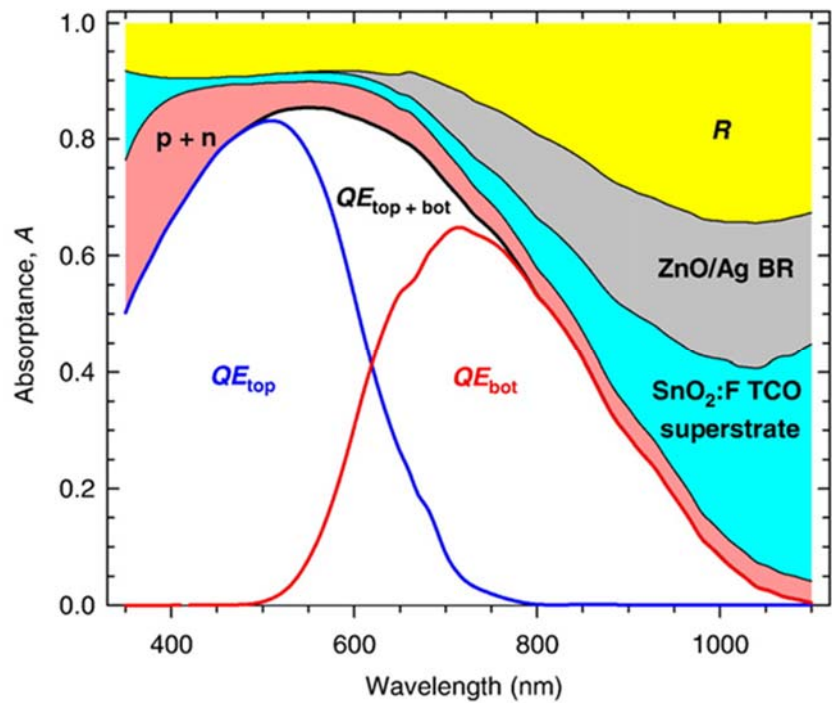


Fig. 1-8. (Color) Optical losses by non-absorber layer in Si thin film solar cells.

From Ref. [16].

1.3. Overview of Transparent Conducting Oxide in Si Thin Film Solar Cells.

The efficiency of a superstrate-type Si thin-film solar cell strongly depends on the quality of the textured TCO layer used for the front electrode material. To improve the cell efficiency, it is necessary to prepare a TCO layer with following two conditions; strong scattering of the incoming light into the silicon absorber layer and favorable physico-chemical properties for the growth of the silicon. For instance, the TCO has to be inert to hydrogen-rich plasmas or act as a good nucleation layer for growth of nanocrystalline material.

For all silicon thin-film solar cells, scattering at interfaces between neighboring layers with different refractive indices and subsequent trapping of the incident light within the silicon absorber layers is crucial to gain a high efficiency. However, absorption coefficients of silicon (about 1.8 eV for standard *a*-Si:H and 1.1 eV for *μc*-Si:H, [17]) are quite lower than that of the other absorber materials (as shown in Fig. 1-9). As a result, in a thin film of not more than several microns thickness incoming light will not be completely absorbed during one single pass. On the other hand, to minimize process time and reduce light-induced degradation of amorphous Si, the absorber layer thickness should be as thin as possible. Hence, for all absorber materials optical absorption inside the silicon layers has to be enhanced by increasing the optical path of solar radiation.

Figure 1-10 show that the enhanced performance by surface-textured ZnO layer. When the rough ZnO film is used as a front layer, light-trapping lengthens the traveling path of photon in the cells such that the absorption ability of the solar cells can be effectively increased. Thus, the resultant quantum efficiency of the cells also increased in the case of using textured ZnO films.

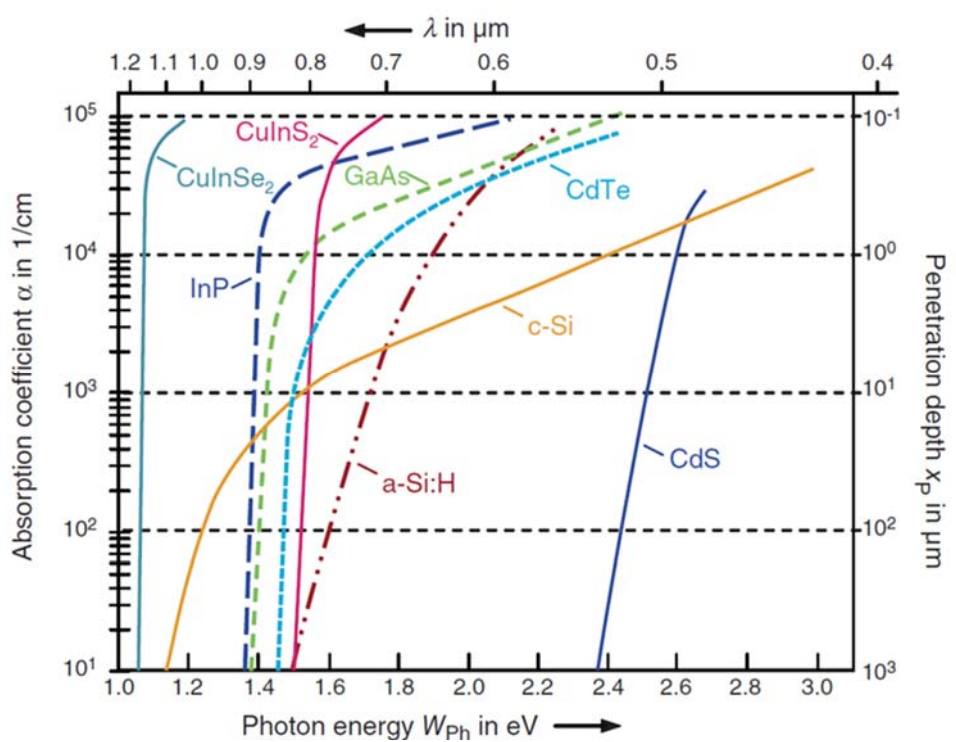


Fig. 1-9. (Color) Absorption coefficient of the different absorber layers in solar cells From Ref. [17]

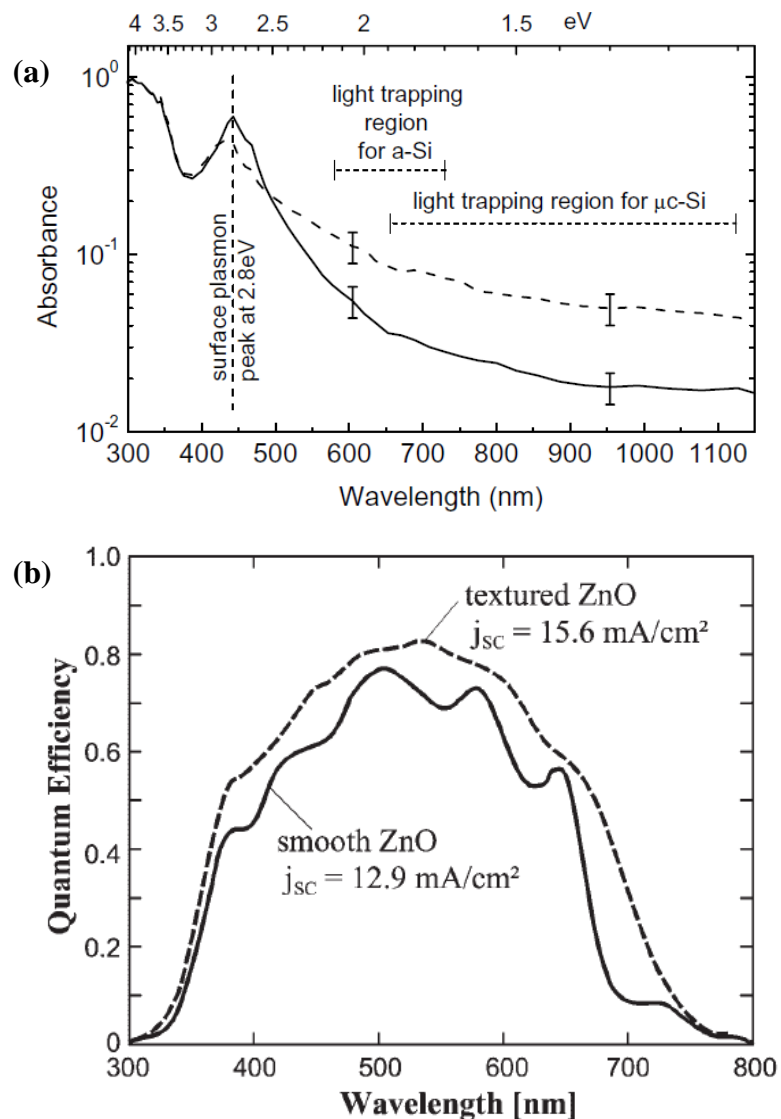


Fig. 1-10. (Color) (a) Absorbance of a smooth (solid line) and textured ZnO layer (dashed line) as a function of wavelength. From Ref. [17] (b) Quantum efficiency of two identically deposited *p-i-n* cells on smooth and etch-textured ZnO. From Ref. [18].

1.3.1. The Factors determining Textured Morphology

As aforementioned, a textured TCO plays an important role in the effective light trapping by transmitting and scattering light into the Si absorber layers. Among the TCOs, the sputtered ZnO:Al films is the representative of front layer in Si thin film solar cell, due to the easy formation of textured morphology and good electrical conductivity [19]. In general, such an adapted surface texture can be obtained by control of sputtering deposition parameters and post wet-chemical etching step in diluted acids or bases. There are 3 major factors determining the textured morphology of ZnO:Al films: (i) deposition pressure, (ii) deposition temperature, (iii) target aluminum concentration.

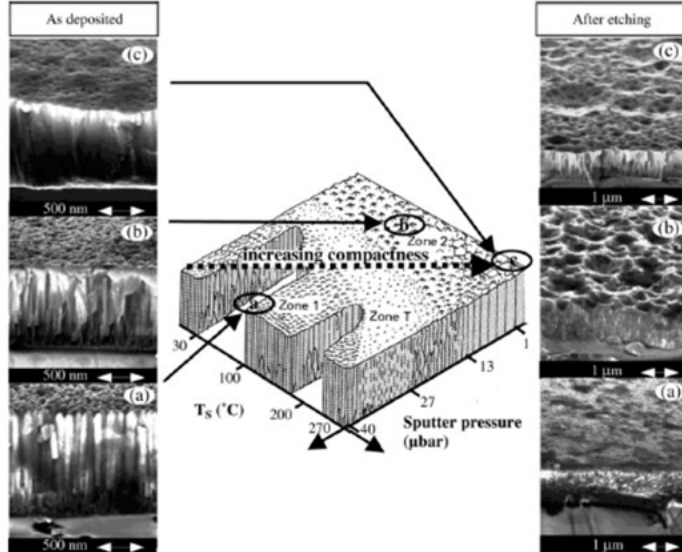
Kluth *et al.* related the influence of pressure and substrate temperature during radio frequency (rf) sputter deposition of ZnO:Al at a fixed alumina content of 2 wt. % in the sputter target to structural properties and post-etching surface topography in a modified Thornton model [20]. They showed that, depending on sputter parameters, crater-like surface topography with typical lateral length scales of 1 - 2 μm and depths of about 200 - 400 nm develops in a self-organized fashion. This etching behavior is affected very sensitively by structural properties of ZnO:Al.

The influence of the target aluminum concentration (TAC) and the substrate temperature on the post-etching surface texture of ZnO:Al films was reported by Berginski *et al.* [21]. Depending on Al concentration in the target and deposition

temperature, three different regimes of etching behavior have been identified, as shown in Fig. 1-12. At low TAC and low substrate temperatures during sputtering, the post-etching surface topography typically comprises a rough surface with small lateral feature sizes of \sim 300 nm and relatively steep edges. At high TAC and high substrate temperatures, after etching we find a rather flat surface with plenty of shallow craters with depths of up to about 100 nm and a few large craters with lateral diameters of up to about 3 μ m and depths limited by film thickness. Between these two parameter regimes, textured surface morphologies are found almost uniformly covered by craters of approximately the same sizes (diameters of about 1 - 3 μ m and depths of about 150 - 400 nm).

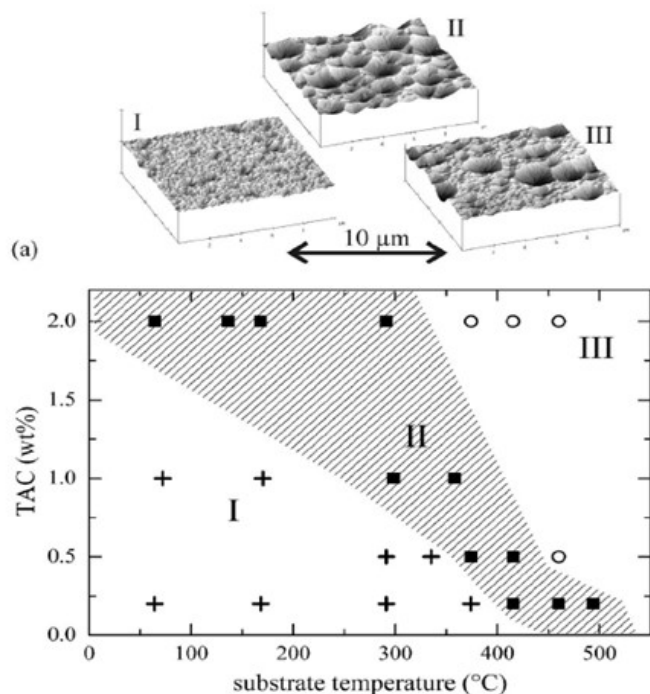
With increasing temperature the growth changes from type I and II to III. The transition temperature for changing the regimes shifts to higher values if TAC is reduced. Consequently, it is suggested that increasing substrate temperature and increasing TAC both similar effects on changing growth conditions. A possible physical explanation relates to the relaxation of built-in stress. Since the ionic radii of Zn^{2+} and Al^{3+} are 0.075 and 0.053 nm, respectively, the addition of Al to ZnO is expected to shorten the *c*-axis length, having an effect on the releasing the residual stress in the as-deposited film. On the other hand, when the Al incorporation is above the critical concentration, excess Al atoms are located at interstitial sites or formed Al-O leading to the enhanced stress in films, as shown in

Fig. 1-13(a) [22]. This stress-release mechanism by doping is close to the substrate temperature effect. During the deposition, the high-energy ions have sufficient energies to bombard the growing films and can be sub-implanted, which lead to the residual stress. With higher substrate temperature, the atoms can easily diffuse to relax the built-in stress (Fig. 1-13(b)) [23,24].



	As-deposited Morphology	After etching Morphology
(a) Low T_s High P	<ul style="list-style-type: none"> Columnar structure with low compactness 	<ul style="list-style-type: none"> Homogeneously etched without craters
(b) Low T_s Low P	<ul style="list-style-type: none"> Dense columnar structure 	<ul style="list-style-type: none"> Regular, rough morphology with large craters
(c) High T_s Low P	<ul style="list-style-type: none"> Highly dense structure 	<ul style="list-style-type: none"> Only partly etched morphology with a few big craters

Fig. 1-11. (Color) The modified Thornton model showing the correlation between deposition parameters, structural film properties, and etching behavior of sputtered ZnO:Al films on glass substrates. From Ref. [20].



	Textured Morphology	Deposition Condition
Type I	<ul style="list-style-type: none"> ▪ Relatively flat surface with small feature size of ~300 nm 	<ul style="list-style-type: none"> ▪ Low TAC (Target Al concentration) ▪ Low dep. Temp.
Type II	<ul style="list-style-type: none"> ▪ Uniform craters (Length: 1-3 μm, depth: ~300 nm) 	<ul style="list-style-type: none"> ▪ TAC at 2 wt. %, ▪ low dep. Temp. (<350°C) ▪ TAC decreased, range of dep. Temp ↓
Type III	<ul style="list-style-type: none"> ▪ Plenty of shallow craters with a few large craters 	<ul style="list-style-type: none"> ▪ High TAC (2 wt.%), ▪ High dep. Temp. (~400°C)

Fig. 1-12. (Color) Schematic illustrations of etching behavior types in a matrix of parameter substrate temperatures and TAC (target Al concentration). From Ref. [21].

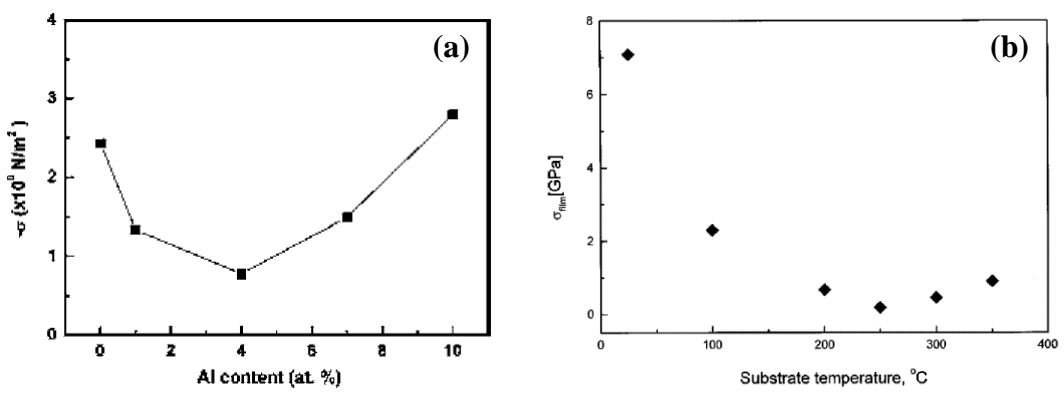


Fig. 1-13. (Color) Residual stress of ZnO:Al films as a function of (a) Al contents and (b) substrate temperature. From Ref. [22] and [23].

1.3.2. The Wet Chemical Etching of ZnO:Al films

For sputtered ZnO:Al films, the surface texture is realized by the combination of an optimized deposition condition and a post deposition wet-chemical etching in diluted acid or bases. Kluth *et al.* reported that textured ZnO:Al films by 0.5 wt. % hydrochloric acid (HCl) showed that a crater-like surface morphology with a typical lateral length scale of 1 - 2 μm and depth of 200 - 400 nm [20]. Berginski *et al.* and Hupkes *et al.* once reported individually that a well-textured ZnO:Al film is able to be performed by 0.5 wt. % HCl solution [21,25]. On the other hands, there has been an attempt to use other etchants for the effective light scattering. Gao *et al.* and Sun *et al.* performed the texturing of ZnO:Al films by NH₄Cl [26]. Owen *et al.* demonstrated etching features by using KOH [27], and Hupkes *et al.* proposed the etching model by comparing of HCl with HF etching [28]. However, these experimental results showed that textured morphology by other etchants show a few craters or smaller size of craters (less than 1 μm), as compared to HCl etching system (Fig. 1-14). Thus, they proposed two step etching method by using both other etchants and HCl which is not adaptable for large-scale manufacturability.

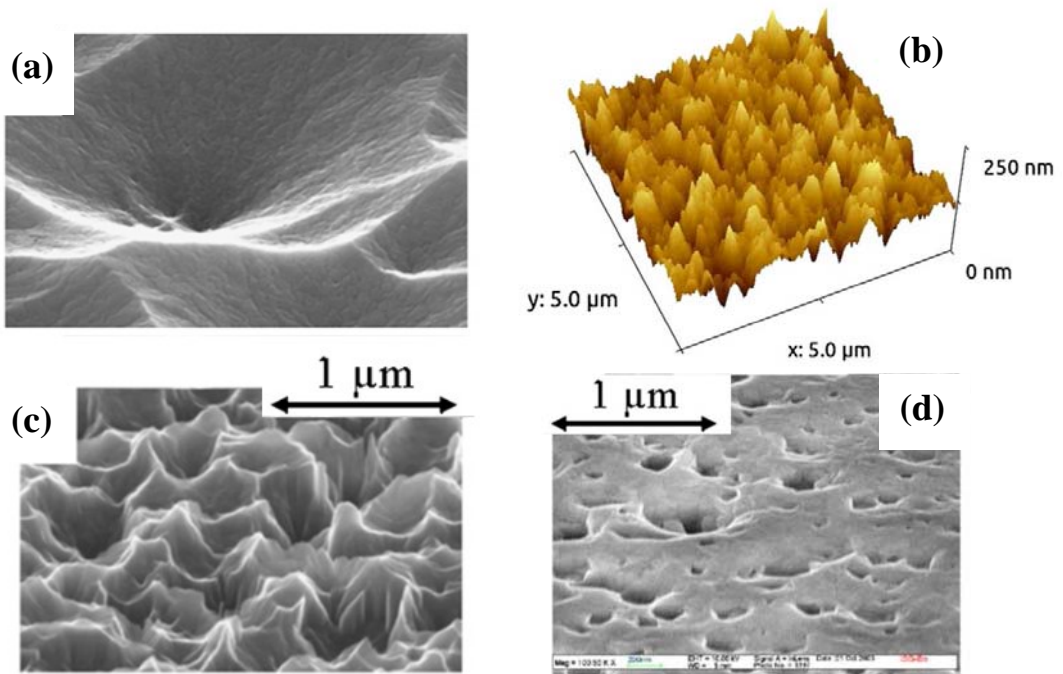


Fig. 1-14. (Color) SEM images of textured Morphology for ZnO:Al films by various etching agents. (a) Etching by 0.1 M HCl for 40 s, (b) by 0.5 M NH₄Cl for 270 s, (c) by 0.3 M HF for 70 s, and (d) by 0.5 M KOH, respectively. From Ref. [26-28].

Chemical etching is widely applied to texturing of sputter-deposited ZnO:Al for light scattering in Si thin film solar cells and therefore, it is necessary to understand the mechanism of structure formation upon etching of polycrystalline ZnO films. ZnO has a wurtzite crystal structure along the *c*-axis, and the (001) and (00-1) planes are Zn- and O-terminated, respectively. The Zn-O bond is primarily ionic, these polar bonds lead to planes of positively charged zinc and negatively charged oxygen atoms perpendicular to the *c*-axis. The etching of single ZnO crystals was reported decades ago, and can be explained on the basis of a dangling bond model [29]. The chemically induced conversion of ZnO into soluble complexes, has been investigated early by Fruhwirth and proceeds according to Eq. 1 in acidic media:



the hydronium ions in acidic solutions readily etching the O-terminated side, while etching only occurs at defects on the Zn-terminated side, as shown in Fig. 1-15.

In the case of a polycrystalline ZnO etching, the deposition conditions of the ZnO films determine the material properties that are modeled by mainly Zn-terminate grains, which are surrounded by grain boundaries of different etch potentials. These potentials depend on the degree of disorder between adjacent grains. The etching agent then defines a threshold by its effective size and mobility. If the etch potential of the grain boundary exceeds this threshold vertical

etching along the grain boundary occurs and craters are formed. Lateral etching is related to the wurtzite structure of ZnO, and its relation to the vertical etch rate defines the shape of craters. The details of etching model for polycrystalline ZnO thin films by J. Hupkes is as follows [30].

Firstly, sputter-deposited polycrystalline ZnO:Al is grown Zn-terminated, and like Zn-terminated single crystals, this (001) crystal plane does not etch in acidic solution, but every grain boundary has a certain potential to be etched. This etching potential describes that the probability of a specific site for crater formation upon etching is attributed to the compactness of the grain boundary. Thus, craters are formed at grain boundaries with less order, having higher potentials for etching than those with more order, as shown in Fig. 1-16(a). The primarily Zn-terminated polycrystalline ZnO surface can be etched only if the etching agent can access a disordered grain boundary to attack other crystal planes.

Secondly, the wet etching of ZnO film in an acidic aqueous solution occurs through the reaction between hydronium ion (H_3O^+) from etchant molecule and oxygen atom from ZnO film surface. This etching reaction will be crystallographic orientation-dependent. The (002) planes of columnar-structured ZnO film with *c*-axis perpendicular to the substrate made up with alternating O and Zn planes, and thus vertical etching reaction is limited by the Zn planes between O planes [29]. On the other hand, lateral etching reaction occurs at the planes, e.g.,

(110), (100), and (200), containing both O and Zn atoms, thus making the etching more facile.

Thirdly, the etchant solution and conditions define an etching threshold. Grain boundaries with etching potentials above the threshold are more actively etched. This threshold depends on the size of etchant complex, as shown in Fig. 1-16(b). Owen *et al.* insists that increasing temperature lowers the threshold, allowing grain boundaries with lower etch potentials to be etched [31]. This is due to the size of the ionic complexes formed by the hydronium ion together with the polar water molecules. At lower temperatures, large complexes are formed with the surrounding water molecules to delocalize the positive charge, as shown in Fig. 1-17 [32,33]. As the solution temperature is increased, the weak hydrogen bonds are broken, effectively making a smaller ion. The smaller water-hydronium complexes are then able to penetrate smaller and thus more grain boundaries or defects than the larger water-hydronium complexes, leading to a higher density of craters.

Lastly, the vertical and horizontal etching rates are also defined by the solution. The vertical etch rate progresses along grain boundaries with etching potentials above the threshold of the solution and is limited by the nature of the grain boundary, as well as the mobility and size of the etching agents. The horizontal etching rate is limited by the concentration of etchants and the crystal structure,

and the etch process stops at the (101) plane. Hupkes *et al.* proposed the etching model by comparing of HCl with HF etching [28], since dissociated HCl and HF molecules will both form large hydrated clusters, the etching behaviors do not only depend on the size of etchant, but also on the tendency of these molecules to dissociate. HCl and HF have acidic dissociation constant of << 0 and 3.2, respectively, thus in HCl solution practically all of the dissolved HCl molecules from large water hydronium complexes. On the other hand, in an HF many of the molecules are not dissociated at a given time and remain relatively small, compared to the water complexes. These small molecules can penetrate defects with even lower etch potential.

Yang's group describes the etching behavior of organic acid [34]. They suggested that due to the bulky, complex structure of organic acids, the movement of water-hydronium complexes is disturbed by the presence of deprotonated organic ligands and thus their accessibility onto the ZnO surface is also limited, in terms of the vertically limited etching characteristics (Fig. 1-18). In addition, unlike monoprotic acid, diprotic oxalic acid in aqueous solution is partially dissociated into hydrogen ion and partially deprotonated oxalic acid species (HC_2O_4^-), thus the incompletely deprotonated species that enter the pore formed would produce additional hydronium ions, causing a rapid lateral etching reaction and consequently widening pores aggressively [35].

In contrast, Q. Jiang *et al.* suggested that the etching reaction and product diffusion co-dominate the process to form craters [36]. Due to accumulated defects and loose characteristics in the grain boundary, it exhibits weakness for the bombardment by H^+ and OH^- , leading to be etched easily in etching agents. However, the columnar grain crystals present a strong resistance due to its few defects and dense characteristics. In this case, the etching reaction dominates the etching process. As a result, the hole will be generated at the initial stage, as illustrated in Fig. 1-19. In the hole, the reaction products cannot diffuse quickly, which prevents the further etching. In this case, the product diffusion dominates the etching process in this hole, which will lower the etching speed of the grain boundary. However, the chemical etching still continues for the grain crystals. As a result, the hole will be wider and wider, and the columnar crystal will be sharper and sharper. With further increasing the etching time, the appearance will become crater-like structure, which is a typical morphology to enhance the light trapping for solar cells.

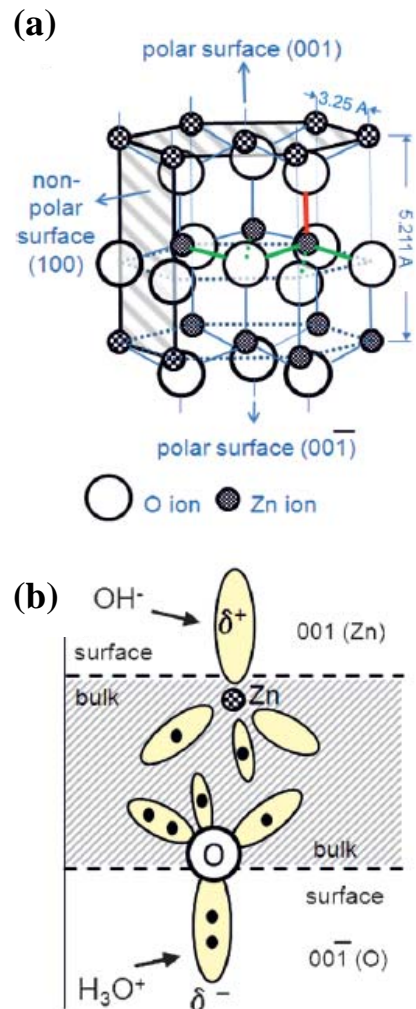


Fig. 1-15. (Color) Schematic illustration of (a) ZnO Wurtzite structure and (b) dangling bond model for etching of a ZnO single crystal. Dotted lines are either projection lines or correspond to bonds that are hidden behind atoms. From Ref. [29].

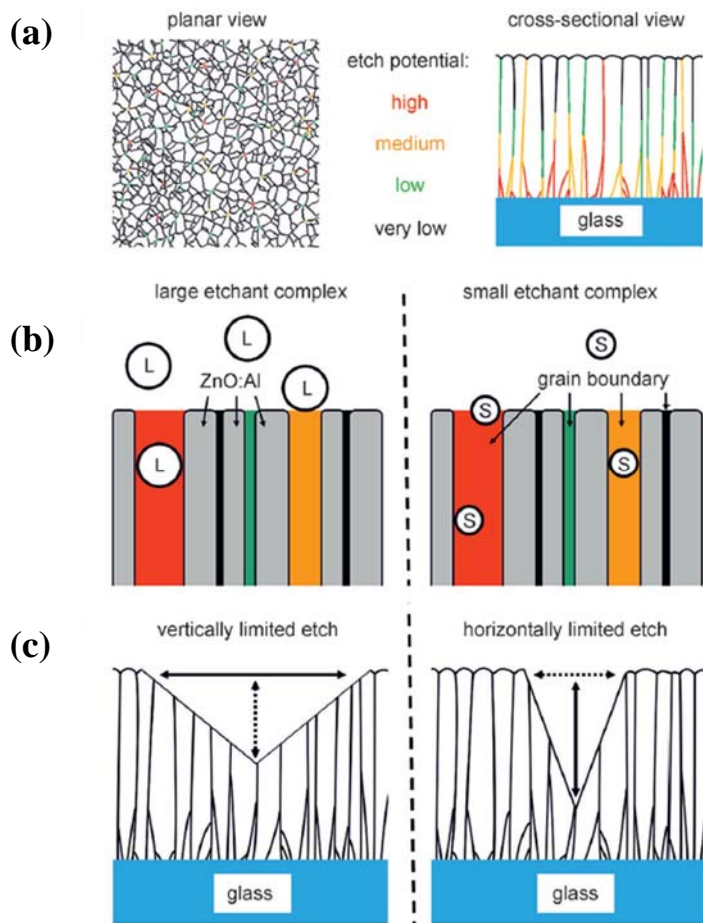


Fig. 1-16. (Color) Schematic illustrations of etching model describing three postulates. a) planar (left) and cross-sectional (right) views of the different etching potentials of the grain boundaries for a ZnO film. (b) interaction of the etchants with the ZnO film depending on the etchant size: large (left) and small etchant (right), at different etching potentials. (c) resulting crater morphologies with vertically (left) and laterally (right) limited etching rates.

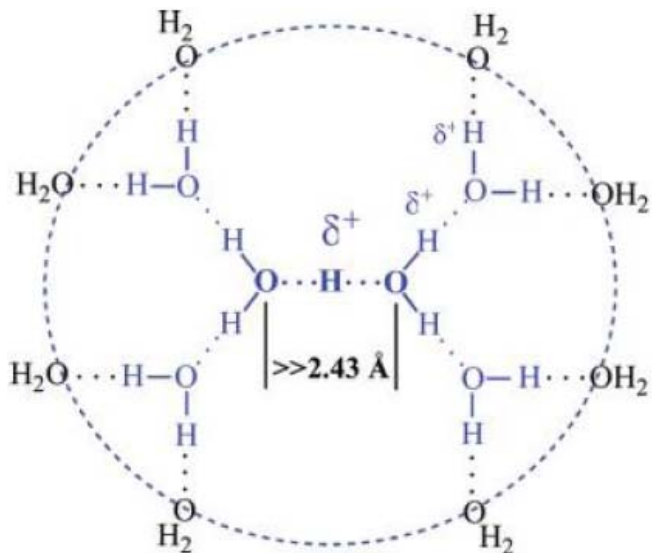


Fig. 1-17. (Color) A proposed structure of water-hydronium complex, $\text{H}(\text{H}_2\text{O})_n^+$, produced when an acid ionizes in water. In case of the value of n in $\text{H}(\text{H}_2\text{O})_n^+$ is 6. From Ref. [32].

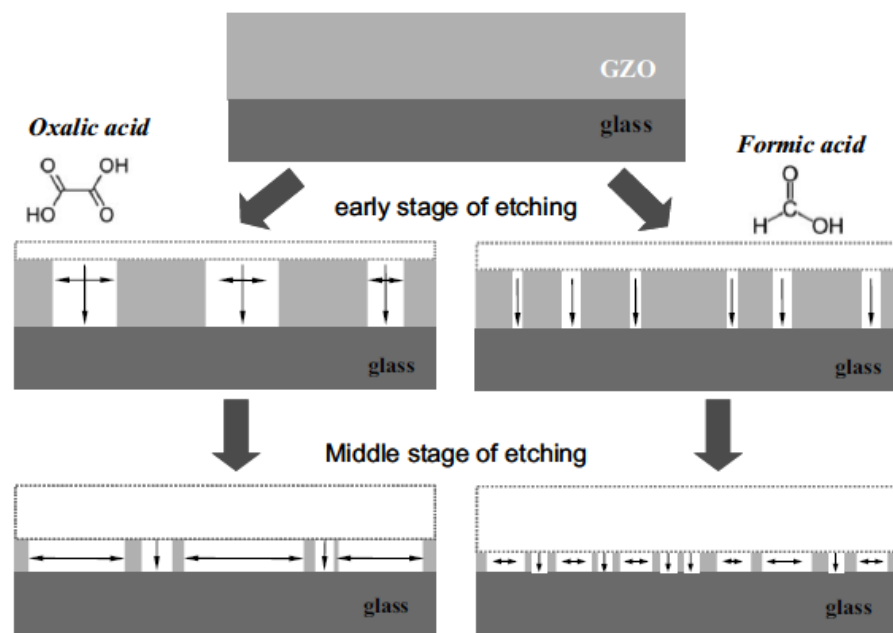


Fig. 1-18. (Color) Schematic representations of etching progress with a period of etching time for oxalic and formic acids. From Ref. [34].

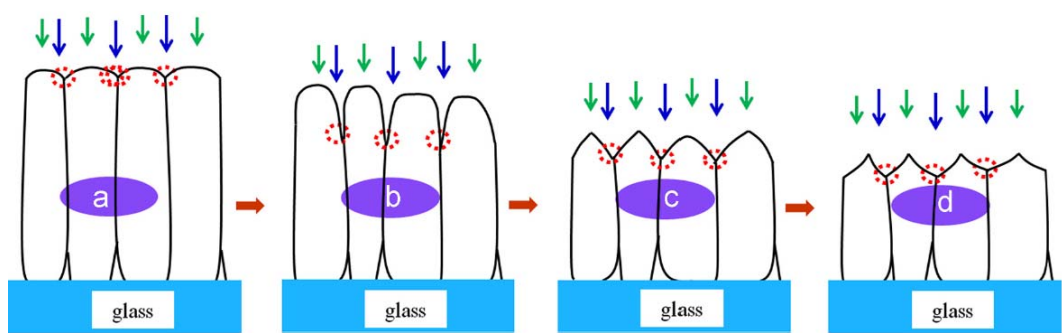


Fig. 1-19. (Color) Schematic illustrations of diagrams of an etching model to illustrate the etching process. The etching reaction and product diffusion co-dominate the process to form crater-like structures. From Ref. [36]

1.4. References

1. K. Yamamoto, A. Nakajima, M. Yoshimi, T. Sawada, S. Fukuda, T. Suezaki, M. Ichikawa, Y. Koi, M. Goto, T. Meguro, T. Matsuda, M. Kondo, T. Sasaki, and Y. Tawada, “A High Efficiency Thin Film Silicon Solar Cell and Module,” *Solar Energy* **77**, 939 (2004).
2. B. van der Ende, L. Arts, and A. Meijerink, “Lanthanide Ions as Spectral Converters for Solar Cells,” *Phys. Chem. Chem. Phys.* **11**, 11081 (2009).
3. J. Nelson, “The Physics of Solar Cells,” *Imperial College Press* UK (2003).
4. S. Kim, J.-W. Chung, H. Lee, J. Park, Y. Heo, and H.-M. Lee, “Remarkable Progress in Thin-film Silicon Solar Cells Using High-efficiency Triple-junction Technology,” *Sol. Energ. Mat. Sol. C.* **119**, 26 (2013).
5. National Center for Photovoltaics, Nat. Renewable Energy Lab., Golden, CO, USA. Chart of best research-cell efficiencies. (2014). [Online]. Available: <http://www.nrel.gov/ncpv>.
6. M. Boccard, P. Cuony, M. Despeisse, D. Domine, A. Feltrin, N. Wyrsch, and C. Ballif, “Substrate dependent stability and interplay between optical and electrical properties in μ c-Si:H single junction solar cells,” *Sol. Energ. Mat. Sol. C.* **95**, 195 (2011).
7. D. Domine, P. Buehlmann, J. Bailat, A. Billet, A. Feltrin, and C. Ballif, “Optical management in high-efficiency thin-film silicon micromorph solar cells with a silicon oxide based intermediate reflector,” *Phys. Stat. Sol. (RRL)* **2**, 163 (2008).

8. F. Meillaud, A. Feltrin, M Despeisse, F-J.Haug, D. Domine, M. Python, T. Soderstrom, P. Cuony, M. Boccard, S. Nicolay, and C. Balif, “Realization of high efficiency micromorph tandem silicon solar cells on glass and plastic substrates: Issues and potential,” *Sol. Energ. Mat. Sol. C.* **95**, 127 (2011).
9. D. Domine, P. Buehlmann, J. Bailat, A. Billet, A. Feltrin, and C. Balif, “Optical management in high-efficiency thin-film silicon micromorph solar cells with a silicon oxide based intermediate reflector,” *Phys. Stat. Sol. (RRL)* **2**, 163 (2008)
10. T. Fujibayashi, T. Matsui, and M. Kondo, “Improvement in quantum efficiency of thin film Si solar cells due to the suppression of optical reflectance at transparent conducting oxide/Si interface by TiO₂/ZnO antireflection coating,” *Appl. Phys. Lett.* **88**, 183508 (2006).
11. O. Berger, D. Inns, and A. G. Aberle, “Commercial white paint as back surface reflector for thin-film solar cells,” *Sol. Energ. Mat. Sol. C.* **91**, 1215 (2007).
12. D. Domine, L. Feitknecht, A. Shah, and C. Balif, “Effect of ZnO layer as intermediate reflector in micromorph solar cells,” *Proceedings of 20th EU Photovoltaic Solar Energy Conference*, pp. 1600.
13. F. Meillaud, A. Feltrin, M. Despeisse, F. Haug, D. Domine, M. Python, T. Soderstrom, P. Cuony, M. Boccard, S. Nicolay, and C. Ballif, “Realization of high efficiency micromorph tandem silicon solar cells on glass and plastic substrates: Issues and potential,” *Sol. Energ. Mat. Sol. C.* **95**, 127 (2011).
14. J. Hupkes, T. Watjen, R. Aubel, R. Schmitz, W. Reetz, and A. Gordijn, “Material study on ZnO/Ag back reflector for silicon thin film solar cells,”

Proceedings of 23rd European Photovoltaic Solar Energy Conference, 1-5 September 2008, Valencia, Spain, pp. 2419.

15. J. Muller, B. Rech, J. Springer, and M. Vanecek, "TCO and light trapping in silicon thin film solar cells," *Sol. Energ. Mat. Sol. C.* **77**, 917 (2004).
16. J. Krc, B. Lipovsek, M. Bokalic, A. Campa, T. Oyama, M. Kambe, T. Matsui, H. Sai, M. Kondo, and M. Topic, "Potential of Thin-Film Silicon Solar Cell by Using High Haze TCO," *Thin Solid Films* **518**, 3054 (2010).
17. L. Schmidt-Mende and J. L. MacManus-Driscoll, "ZnO-Nanostructures, Defects, and Devices," *Mater. Today* **10**, 40-48 (2007).
18. A. V. Shah, H. Schade, M. Vanecek, J. Meier, E. Vallat-Sauvain, N. Wytsch, U. Kroll, C. Droz, and J. Bailat, "Thin-Film Silicon Solar Cell Technology," *Prog. Photovoltaics*, 12, 113 (2004).
19. O. Berger, D. Inns, and A. G. Aberle, "Commercial white paint as back surface reflector for thin-film solar cells," *Sol. Energ. Mat. Sol. C.* **91**, 1215 (2007).
20. O. Kluth, G. Schöpe, J. Hüpkes, C. Agashe, J. Müller, and B. Rech, "Modified Thornton model for magnetron sputtered zinc oxide: film structure and etching behavior," *Thin Solid Films* **442**, 80 (2003).
21. M. Berginski, J. Hüpkes, M. Schulte, G. Schöpe, H. Stiebig, and B. Rech, "The Effect of Front ZnO:Al Surface Texture and Optical Transparency on Efficient Light Trapping in Silicon Thin-Film Solar Cells," *J. Appl. Phys.* **101**, 074903-1 (2002).

22. J. G. Lu, Z. Z. Ye, Y. J. Zeng, L. P. Zhu, L. Wang, J. Yuan, B. H. Zhao, and Q. L. Liang, “Structural, Optical, and Electrical Properties of (Zn, Al) O Films over a Wide Range of Compositions,” *J. Appl. Phys.* **100**, 073714-1 (2006).
23. M. Chen, Z. L. Pei, X. Wang, C. Sun, and L. S. Wen, “Structural, Electrical, and Optical Properties of Transparent Conductive Oxide ZnO:Al Films Prepared by dc Magnetron Reactive Sputtering,” *J. Vac. Sci. Technol. A* **19**, 963 (2001).
24. Y. Wang, Y. Gu, S. Peng, W. Ding, H. Wang, and W. Chai, “Influence of Substrate Temperature on Surface Textured ZnO:Al Films Etched with NaOH Solution,” *Appl. Surf. Sci.* **257**, 8044 (2011).
25. J. Hüpkes, B. Rech, O. Kluth, T. Repmann, B. Zwaygardt, J. Müller, R. Drese, and M. Wuttig, “Surface textured MF-sputtered ZnO films for microcrystalline silicon-based thin-film solar cells,” *Sol. Energ. Mat. Sol. C* **90**, 3054 (2006).
26. S. Fernandez, O. Abril, F. Naranjo, and J. Grandia, “Etching Process Optimization Using NH₄Cl Aqueous Solution to Texture ZnO:Al Films for Efficient Light Trapping in Flexible Thin Film Solar Cells,” *Thin Solid Film* **520** 4144 (2012).
27. J. Hüpkes, B. Rech, S. Calnan, O. Kluth, U. Zastrow, H. Siekmann, and M. Wuttig, “Material Study on Reactively Sputtered Zinc Oxide for Thin Film Silicon Solar Cells,” *Thin Solid Films* **502**, 286 (2006).
28. B. Rech, J. Muller, T. Repmann, O. Kluth, T. Roschek, J. Hüpkes, H. Stiebig, and W. Appenzeller, “Amorphous and Microcrystalline Silicon Based Solar

Cells and Modules on Textured Zinc Oxide Coated Glass Substrates," *Mat. Res. Soc. Symp. Proc.* **761**, A3.1 (2003).

29. K. Ellmer, A. Klein, and B. Rech, "Transparent Conductive Zinc Oxide: Basics and Applications in Thin Film Solar Cells," *Springer* (2008).
30. J. Hüpkes, J. I. Owen, S. E. Pust, and E. Bunte, "Chemical Etching of Zinc Oxide for Thin-Film Silicon Solar Cells," *ChemPhysChem* **13**, 66 (2012).
31. J. I. Owen, S. E. Pust, E. Bunte, and J. Hupkes, "ZnO Etch-Feature Control via Concentration and Temperature of Various Acids," *ECS J. Solid State SC.* **1**, P11 (2012).
32. E. S. Stoyanov, I. V. Stoyanova, and C. A. Reed, "The Structure of the Hydrogen Ion (H_{ad}^+) in Water," *J. Am. Chem. Soc.* **132**, 1484 (2010).
33. S. S. Iyengar, M. Petersen, T. F. Day, C. J. Burnham, V. E. Teige, and G. A. Voth, "The Properties of Ion-Water Clusters. I. The Protonated 21-Water Cluster," *J. Chem. Phys.* **123**, 084309 (2005).
34. D. Lee, S. Lee, J. Bang, H. Yang, "Wet chemical etching of transparent conducting Ga-doped ZnO thin films by oxalic and formic acid," *J. Electrochem. Soc.* **156**, D211 (2009).
35. D. Lee, J. Bang, M. Park, J.-H. Lee, and H. Yang, "Organic Acid-Based Wet Etching Behaviors of Ga-doped ZnO Films Sputter-Deposited at Different Substrate Temperature," *Thin Solid Films* **518**, 4046 (2010).
36. Q. Jiang, J. Lu, J. Zhang, Y. Yuan, H. Cai, C. Wu, R. Sun, B. Lu, X. Pan, and Z. Ye, "Texture Surfaces and Etching Mechanism of ZnO:Al Films by a Neutral Agent for Solar Cells," *Sol. Energ. Mat. Sol. C.* **130**, 264 (2014).

Chapter 2.

*Organic Acid Texturing of Transparent Electrodes Toward Broadband Light Trapping in Thin Film Solar Cells

2.1. Introduction

The key challenges for the solar-cell developments lie in the improvement of power-conversion efficiency and reduction of fabrication cost [1-3]. For enhancing the power-conversion efficiency, much research has been focused on light trapping to fully utilize broadband light with minimum optical losses [4-6]. Novel light-trapping methods using photonic structures or plasmonic effects are being continuously reported [7,8]. However, these methods require additional steps or materials inducing cost concerns inevitably questioning the possibility of the large-scale manufacturability.

Especially for Si thin-film solar cells with a superstrate configuration, light-trapping capability is mainly determined by the surface texturing of the front TCO [9-13]. The scattering by the rough surface increases the optical-path lengths, leading to high absorption in the active semiconductor layers, thereby enhancing

*The work presented in Chapter 2 currently in preparation entitled,
“Organic Acid Texturing of Transparent Electrodes Toward Broadband Light Trapping in Thin Film Solar Cells,”
Woojin Lee, Taehyun Hwang, Sangheon Lee, Seung-Yoon Lee, Joonhyeon Kang, Byungho Lee, Jinhyun
Kim, Taeho Moon,* and Byungwoo Park.*

the power-conversion efficiency [14,15]. Compared to the conventional SnO₂:F, ZnO-based TCOs have received strong attention because of the large feature size from surface texturing by wet-chemical etching, enabling more efficient light scattering [15-21].

The surface morphology by wet etching depends on the nanostructures of TCO [22,23]. In manufacturing, however, the nanostructural control of TCO is pretty limited due to the consideration of electrical conductivity and high throughput. Therefore, the tunability of surface texturing by simple etching for the synthesized TCO nanostructures offers a great merit for the strategy of TCO development with superior light-scattering performance.

In this chapter, an organic acid for the surface texturing of ZnO-based TCO is introduced as an alternative to conventional HCl. The enhancement of light scattering by oxalic acid is demonstrated without any deterioration of transparency or resistance. We believe that the organic-acid texturing can be easily adopted in manufacturing process via simple substitution of the wet etchant, which is a cost effective light-trapping technique toward high efficiency solar cells. A light-scattering model can be easily optimized with the control of etching anisotropy for texturing of the TCO.

2.2. Experimental Section

The ZnO:Al films of 1.8 μm thickness were deposited on glass substrate (Corning 1737) by rf magnetron sputtering using a ZnO:Al target (1 wt. % Al_2O_3). Sputtering was performed at 400°C under an Ar atmosphere with an operating pressure of 5 mTorr and rf power of 75 W. As-grown ZnO:Al films showed the resistivity of $\sim 8 \times 10^{-4} \Omega \text{ cm}$. Surface texturing was performed by means of wet-chemical etching using oxalic acid (0.02 M) and HCl (0.1 M) at room temperature in order to compare the light-scattering properties.

The electrical properties of the films were measured by 4-point probe, and the morphologies of etched ZnO:Al films were evaluated over a scan area of $10 \times 10 \mu\text{m}^2$ by atomic force microscopy (AFM, SPA-400: Seiko Instrument). The normal incidence and total transmission spectra of surface-textured thin films were carried out with a UV-Vis spectrometer (Lambda 35: Perkin Elmer) equipped with an integrating sphere. From these measurements, the transmission haze parameter was determined by the ratio of diffused to total transmittance ($T_{\text{diffused}}/T_{\text{total}}$).

2.3. Results and Discussion

Texturing morphologies etched by conventional HCl and oxalic acid were compared by SEM, as shown in Fig. 2-1(a) and (b). Notably, the difference on crater shape is shown between two etching systems. In the case of HCl, sharp

craters are shown as reported by many researchers [23-26]. Meanwhile, in the case of oxalic acid, the craters of round morphologies are observed. Basically, texturing morphology formed by wet etching is determined by the difference of etching rates between grain and grain boundary, thus the crater-shape difference indicates that relative etching rates for grain and grain boundary are changed between two etching systems. From the round morphology, we can know that oxalic acid has faster lateral etching rate for grain (for pore widening) compared to the vertical etching rate through grain boundary. The exact comparison of the crater dimensions between two etching systems was difficult by SEM imaging, due to the distribution of crater sizes. Therefore, surface roughness was characterized by AFM in order to statistically quantify the crater morphologies. A rough surface can be two-dimensionally characterized by RMS value (vertical roughness) and correlation length (lateral roughness) [24,25]. The RMS roughness σ_{rms} is defined as:

$$\sigma_{rms}^2 = \langle z(x,y)^2 \rangle - \langle z(x,y) \rangle^2 \quad (1)$$

where $z(x,y)$ is surface-height distribution and $\langle \rangle$ represents an average value. The lateral correlation from rough surfaces can be obtained by the autocorrelation function [24-27]:

$$C(\tau_x, \tau_y) = \lim_{L_x, L_y \rightarrow \infty} \frac{1}{4L_x L_y \sigma_{rms}^2} \iint_{-L_y-L_x}^{L_y L_x} z(x,y) z(x + \tau_x, y + \tau_y) dx dy, \quad (2)$$

where L_x and L_y are the scanning lengths for the $z(x,y)$ profile. After fitting the autocorrelation function with a Gaussian function, $C(\tau) = \exp(-\tau^2 / a_{corr}^2)$ where $\tau^2 = \tau_x^2 + \tau_y^2$, the lateral correlation length a_{corr} can be extracted [24]. Figures 2-2(a) - (c) show a typical procedure for the extraction of σ_{rms} , $C(\tau)$, and a_{corr} and the AFM data. the AFM data ($8 \times 8 \mu\text{m}^2$) are scanned at three different areas for each textured film.

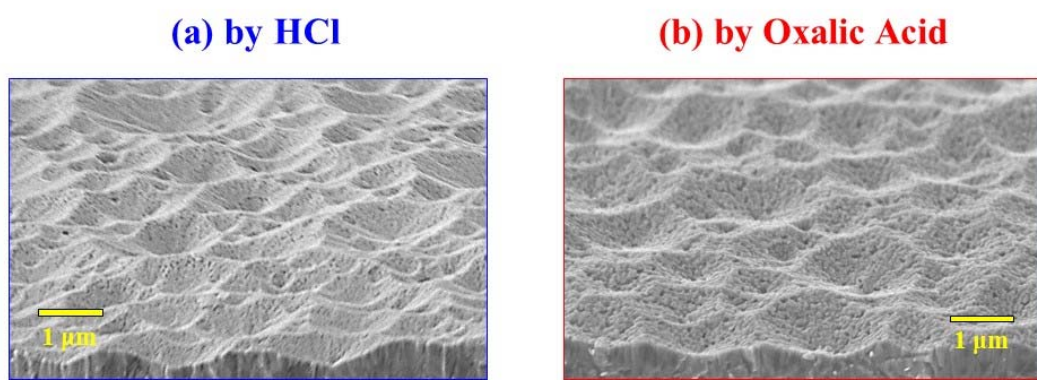


Fig. 2-1. (Color) SEM images of the ZnO:Al thin films textured by (a) HCl and (b) oxalic acid.

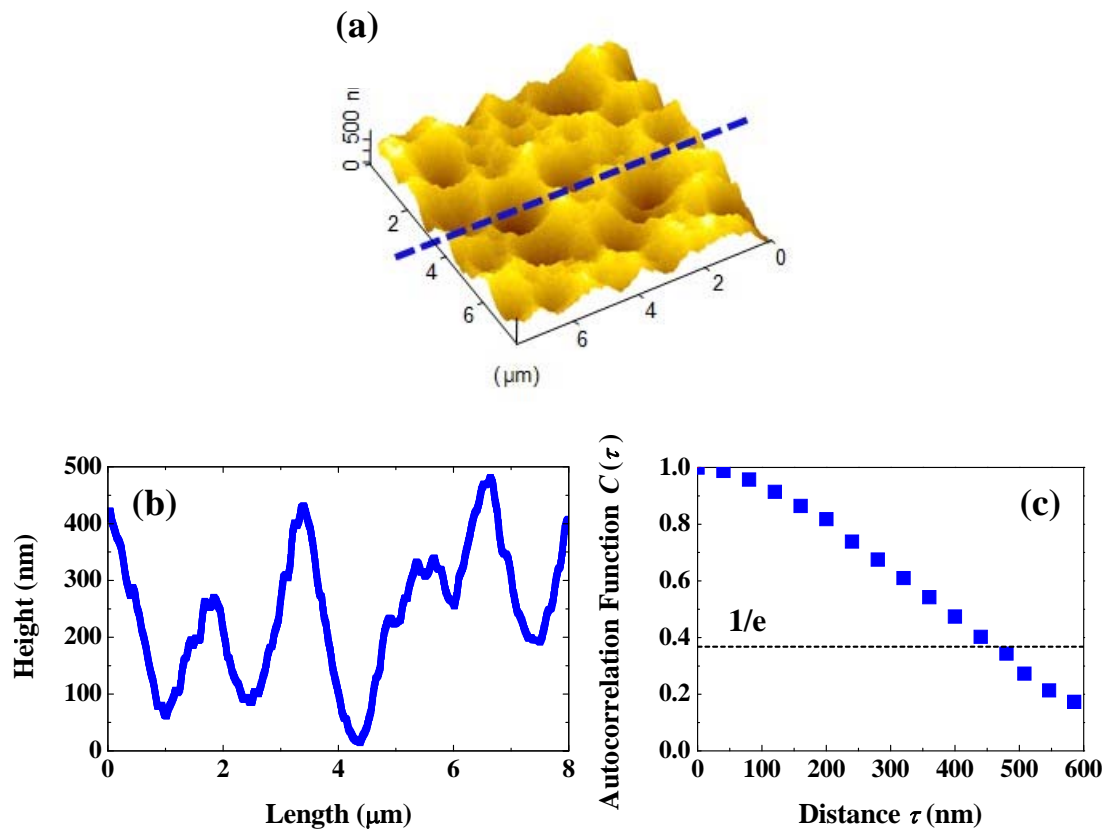


Fig. 2-2. (Color) (a) AFM image of a ZnO:Al thin film textured by oxalic acid. (b) Sectioned surface profile from the AFM image. (c) Normalized autocorrelation function from the surface profile.

The etching-morphology evolution was investigated through the extraction of σ_{rms} and a_{corr} values for the films textured at different etching times, and the obtained parameters with corresponding cross-sectional profiles and normalized autocorrelation functions are presented in Fig. 2-3, 2-4 and 2-5. Notably, two distinctive features are shown by oxalic acid, compared to HCl. First, much slower etching rate is found. Second, larger correlation length at the similar RMS value (e.g. Figs. 2-3(c) and 2-4(e)) is observed, indicating the overall increase of lateral feature size. As expected by the crater shape from SEM imaging, the increase of lateral feature size clearly confirms that oxalic acid has faster lateral etching rate for grain (or slower vertical etching rate for grain boundary). The reasons why oxalic acid ($H_2C_2O_4$) exhibits different etching behavior can be understood by the bulky structure of deprotonated species ($HC_2O_4^-$) inhibiting the accessibility of water-hydronium complexes onto the grain boundary of ZnO, which results in slower vertical etching rate for grain boundary, and lateral feature size with round morphology is attributed that partially deprotonated species ($HC_2O_4^-$) can enter the pore formed would produce additional hydronium ions, causing a rapid lateral etching [28].

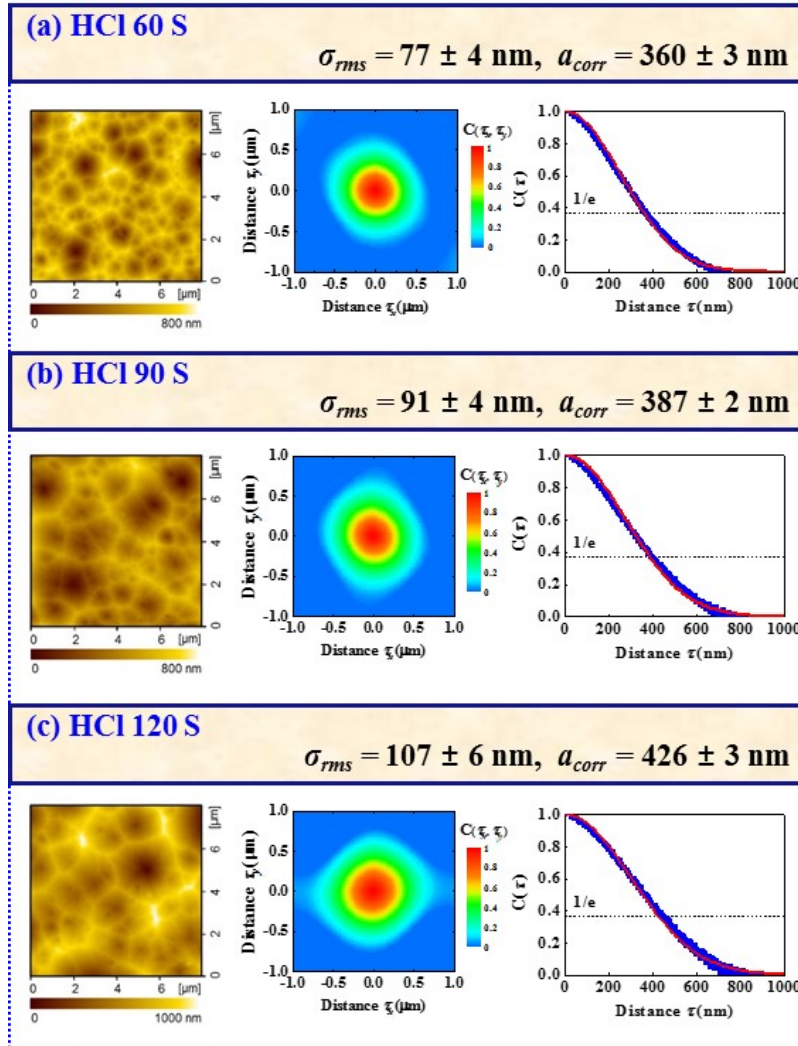


Fig. 2-3. (Color) Extraction of vertical roughness (σ_{rms}) and lateral correlation length (a_{corr}) from AFM data. Etching time dependency by HCl (a-c). For each panel, AFM image (left), 2-D contour plot of autocorrelation function (center), and the autocorrelation function averaged over the azimuth angle ($\tau^2 = \tau_x^2 + \tau_y^2$), with the Gaussian fitting (right).

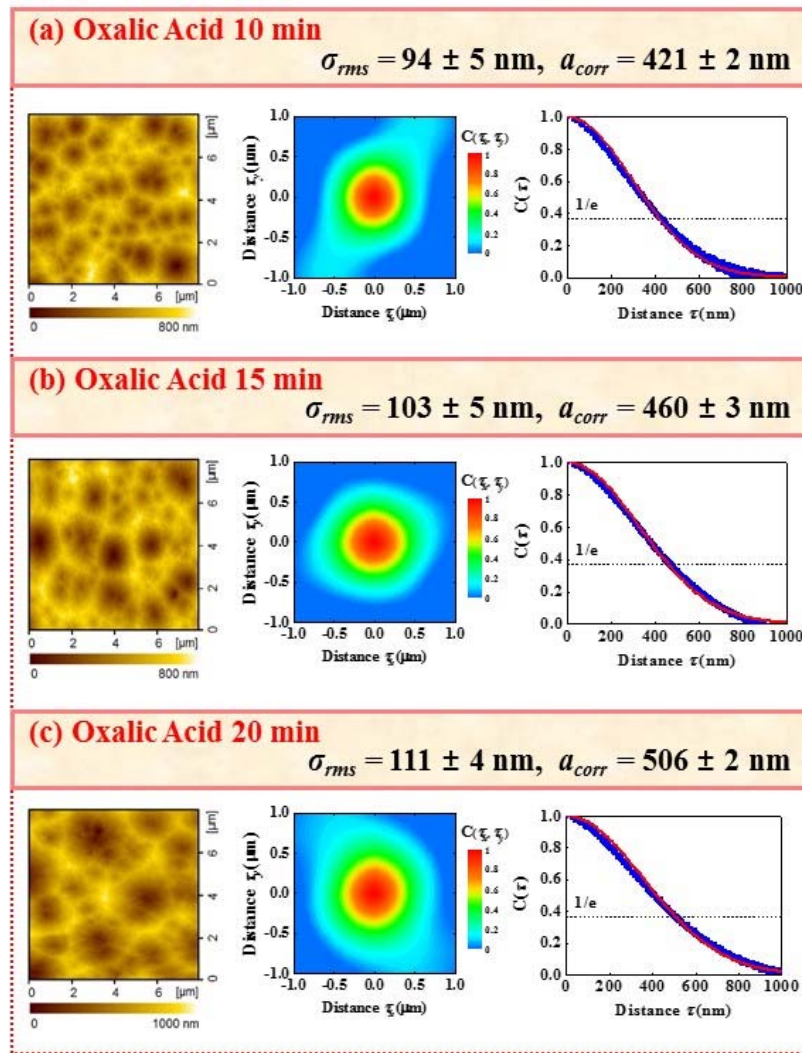


Fig. 2-4. (Color) Extraction of vertical roughness (σ_{rms}) and lateral correlation length (a_{corr}) from AFM data. Etching time dependency by oxalic acid (a-c). For each panel, AFM image (left), 2-D contour plot of autocorrelation function (center), and the autocorrelation function averaged over the azimuth angle ($\tau^2 = \tau_x^2 + \tau_y^2$), with the Gaussian fitting (right).

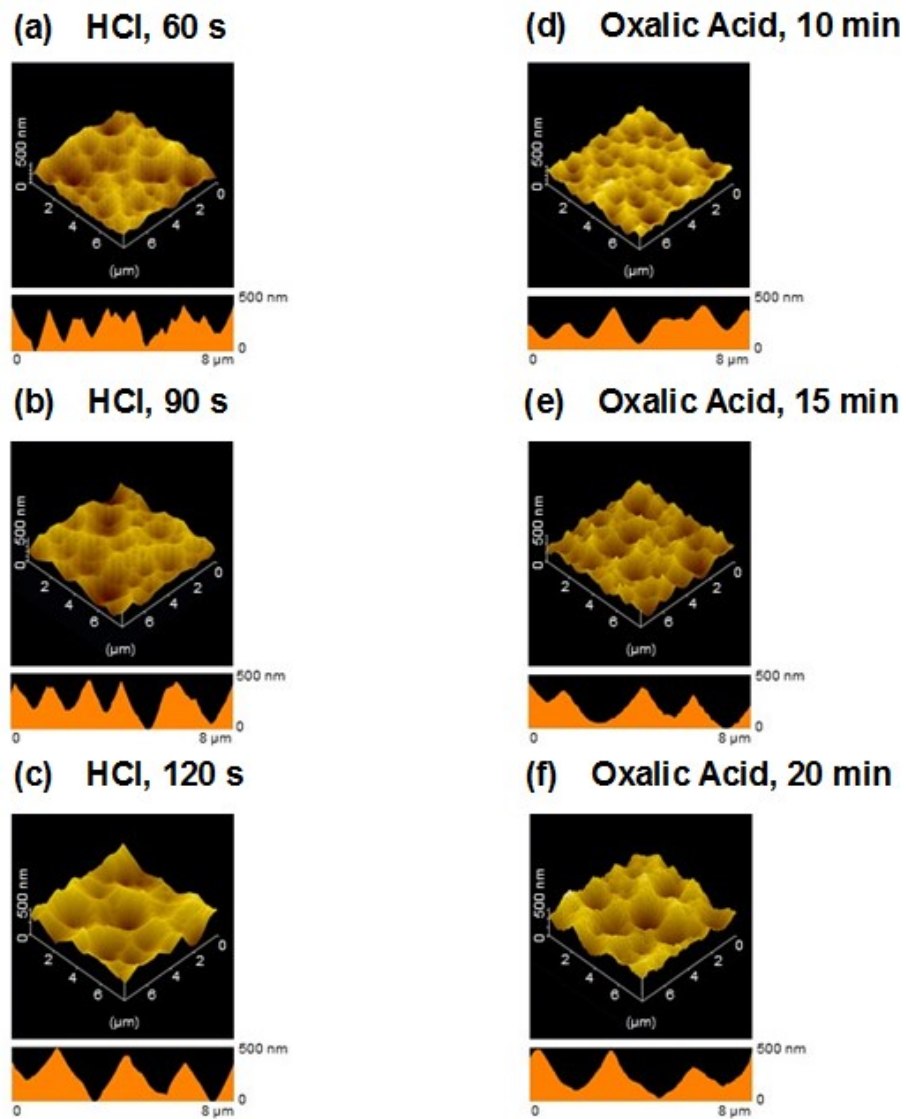


Fig. 2-5. (Color) Cross-sectional AFM images of the textured ZnO:Al films.

(a-c) Etching-time dependence by HCl. (d-f) Etching-time dependence by oxalic acid.

The optical and electrical properties were investigated for various samples, and were correlated with the surface-morphology information, as shown in Fig. 2-6. Figures 2-6(a) and 2-6(b) show the total transmittance and haze characteristics for the films textured by HCl and oxalic acid, respectively, at different etching times. The haze is determined from the ratio of diffuse to total transmittance ($T_{diffused}/T_{total}$). Even though no significant differences in the total transmittances are observed, the haze values increase with the etching time due to the crater evolution. Interestingly, the textured ZnO:Al films by oxalic acid show higher haze over the whole wavelength range compared to those by HCl. Particularly at the long wavelength region, the haze increase becomes more significant. Electrical performance (sheet resistance) also change by etching, therefore the performances of TCOs textured by different etchants should be considered in the aspects of both optical and electrical properties. Figure 2-6(c) shows haze (at $\lambda = 1000$ nm) vs. sheet resistance for two systems. The clear trend showing superior light-scattering performance by oxalic acid is confirmed, and the absolute haze increase of ~8% is observed at the given sheet resistance.

The light-scattering behavior of textured films can be theoretically understood by the coupling between the rough surface and light. Modified scalar scattering theory as a function of vertical roughness (σ_{rms}) and lateral correlation length (a_{corr}) by Lin's group is used to understand the light-scattering performance [24]:

$$H_T = \frac{T_{\text{diffused}}}{T_{\text{total}}} = \frac{(1 - \exp^{-(2\pi\sigma_{\text{rms}}/\lambda)^2(n-1)^2})(1 - \exp^{-(\pi a_{\text{corr}}/\lambda)^2})}{1 - \exp^{-(\pi a_{\text{corr}}/\lambda)^2}(1 - \exp^{-(2\pi\sigma_{\text{rms}}/\lambda)^2(n-1)^2})}, \quad (3)$$

where λ and n are the wavelength of light and the index of refraction of TCO, respectively. For the index of refraction of ZnO films, we used the experimental results by Washington *et al.* [29]. For the validity of this formula, wavelength-dependent haze curves were fitted, as shown in Figs. 2-7(a). It is found that the surface-roughness parameters by the fitting are in good agreement with those extracted from the AFM data, as summarized in Table 2-1, and small discrepancies are understood by the difference in the scan size of two measurement systems.

To have a better insight into the effect of crater morphology on the light scattering, haze contour (Eq. (3)) is plotted as a function of two surface parameters, σ_{rms} and a_{corr} , at various wavelengths (Fig. 2-8), and are compared with the surface parameters obtained from AFM. At the short wavelength $\lambda = 400$ nm, vertical roughness is the factor affecting the haze values, while the effect by the lateral correlation length looks negligible. The contribution of lateral correlation on haze becomes stronger with the increase of wavelength, and the superior haze at $\lambda = 1000$ nm by oxalic acid can be explained by the crater-size effect (i.e., increase of lateral feature size).

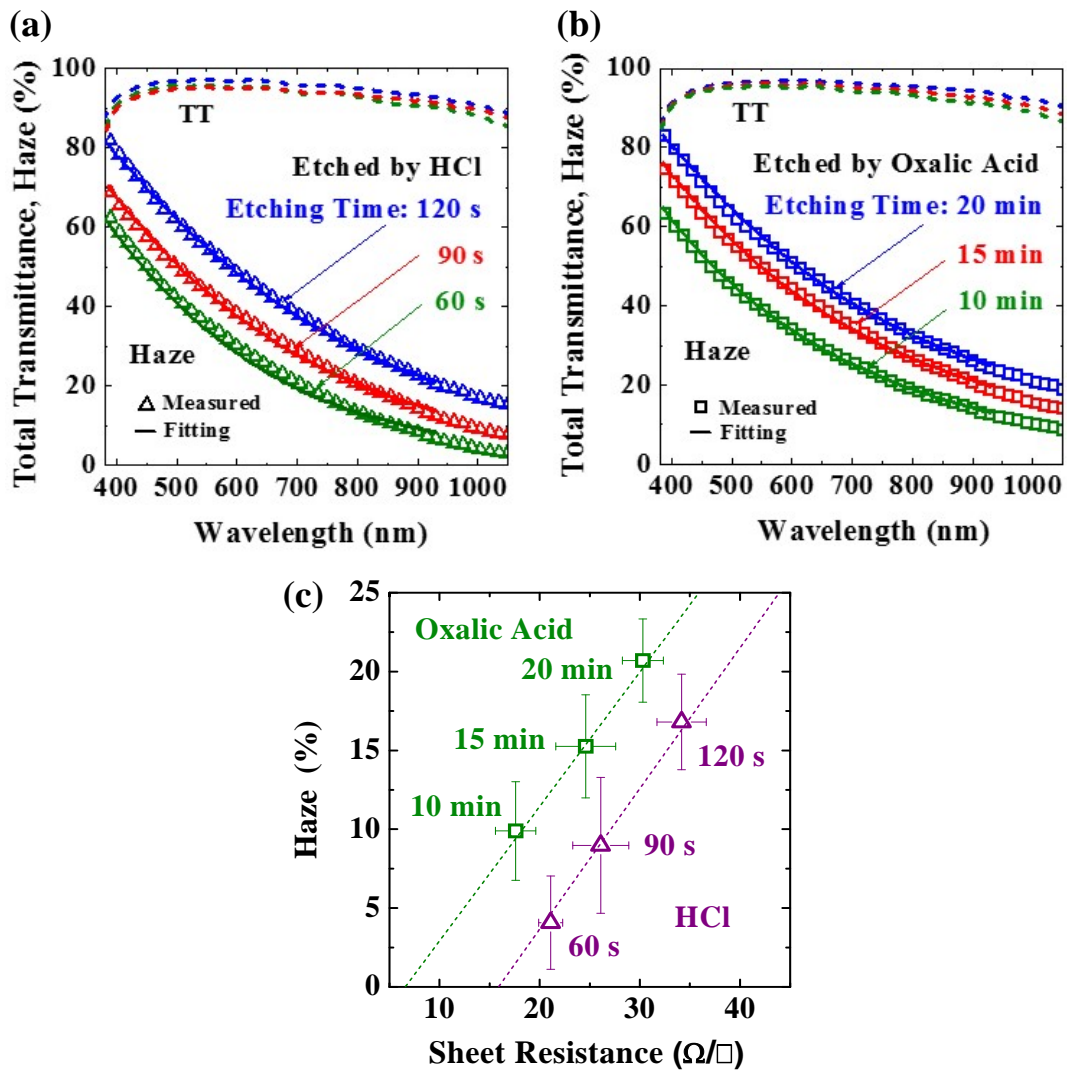


Fig. 2-6. (Color) Optical and electrical properties for the textured ZnO:Al films.

- (a-b) Total transmission and haze curves by (a) HCl and (b) oxalic acid.
- (c) A plot of haze (at $\lambda = 1000$ nm) vs. sheet resistance.

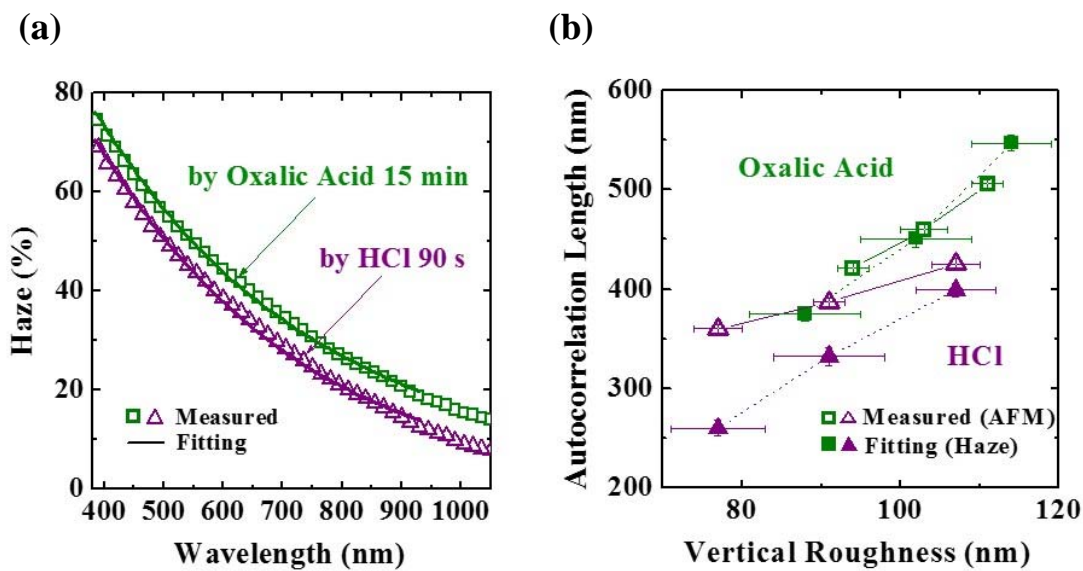


Fig. 2-7 (Color) (a) Haze curves etching by HCl (90 s) and oxalic acid (15 min).

The solid lines are represented the fitting by Eq. (3). (b) Comparison of surface roughness parameters from AFM and haze.

Table. 2-1. Comparison of the surface parameters obtained from the AFM and haze data.

	Vertical Roughness (σ_{rms})		Autocorrelation Length (a_{corr})	
	AFM	Haze	AFM	Haze
HCl 60 s	77 ± 4 nm	84 ± 9 nm	360 ± 3 nm	260 ± 8 nm
90 s	91 ± 4 nm	95 ± 7 nm	387 ± 2 nm	332 ± 9 nm
120 s	107 ± 6 nm	111 ± 5 nm	426 ± 3 nm	399 ± 7 nm
Oxalic Acid 10 min	94 ± 5 nm	88 ± 7 nm	421 ± 2 nm	375 ± 7 nm
15 min	103 ± 5 nm	102 ± 7 nm	460 ± 3 nm	451 ± 9 nm
20 min	111 ± 4 nm	114 ± 6 nm	506 ± 2 nm	547 ± 8 nm

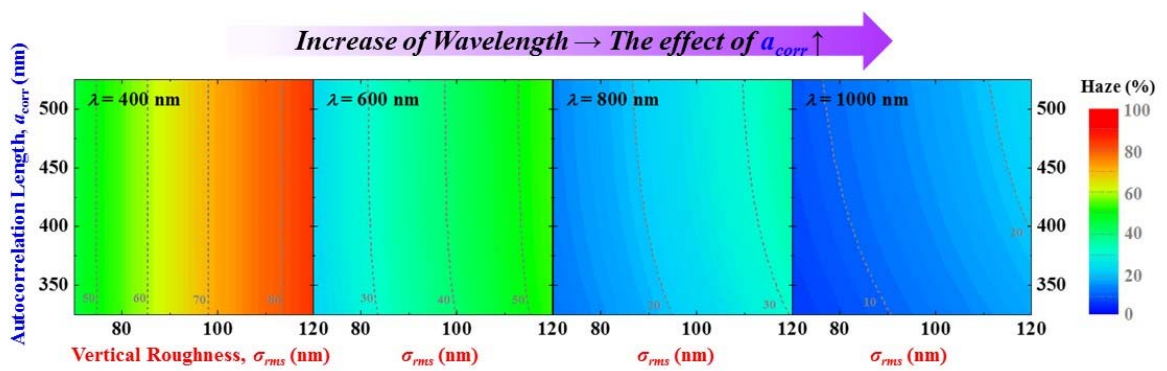
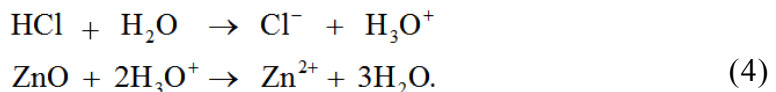
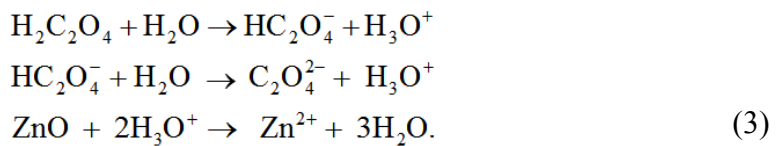


Fig. 2-8. (Color) Haze-contour plot as a function of σ_{rms} and a_{corr} at different wavelengths (from Eq. (3)).

Based on the surface parameter analyses, we concluded that oxalic acid has the higher lateral to vertical etching ratio than HCl. Regarding the crater formation mechanisms, it is generally believed that grain boundaries having the highest etching potential (the highest grain-boundary interfacial energy) are first etched. Then, diffusion of etching reactants and byproducts is allowed through the vertical opening, followed by lateral etching into grains [30,31]. Repetitive processes lead to the evolution of crater morphology with continuous Zn²⁺ dissolution, and competition between two etching speeds will determine the crater shape of the textured TCO films. Based on these assumptions, a phenomenological model is suggested to explain the distinctive crater evolution mechanisms in oxalic acid (Fig. 4). If sufficient electrolyte can continue to be supplied into the pores produced by the etching of weak grain boundaries, ZnO can be effectively dissolved along the various grain boundaries, leading to fast vertical etching. While, if it is hard for the reactants to reach the narrow grain-boundary pores, etching reaction will be limited by the mass transport, which retards the vertical etching. In the acidic environment, etching reaction by oxalic acid (H₂C₂O₄) and HCl, respectively, can be expressed as:



It is expected that diffusion issue of oxalic acid ($\text{H}_2\text{C}_2\text{O}_4$) or deprotonated species (HC_2O_4^- and $\text{C}_2\text{O}_4^{2-}$) into the etched grain-boundary pores is crucial, compared to the HCl etching having relatively smaller size of reactants (Cl^-). Limited mass transport of oxalic acid will lead to the slowing down of vertical etching through the high-energy grain boundaries, and lateral etching to grains is simultaneously accompanied, which will eventually lead to larger crater formation at given etching depth.

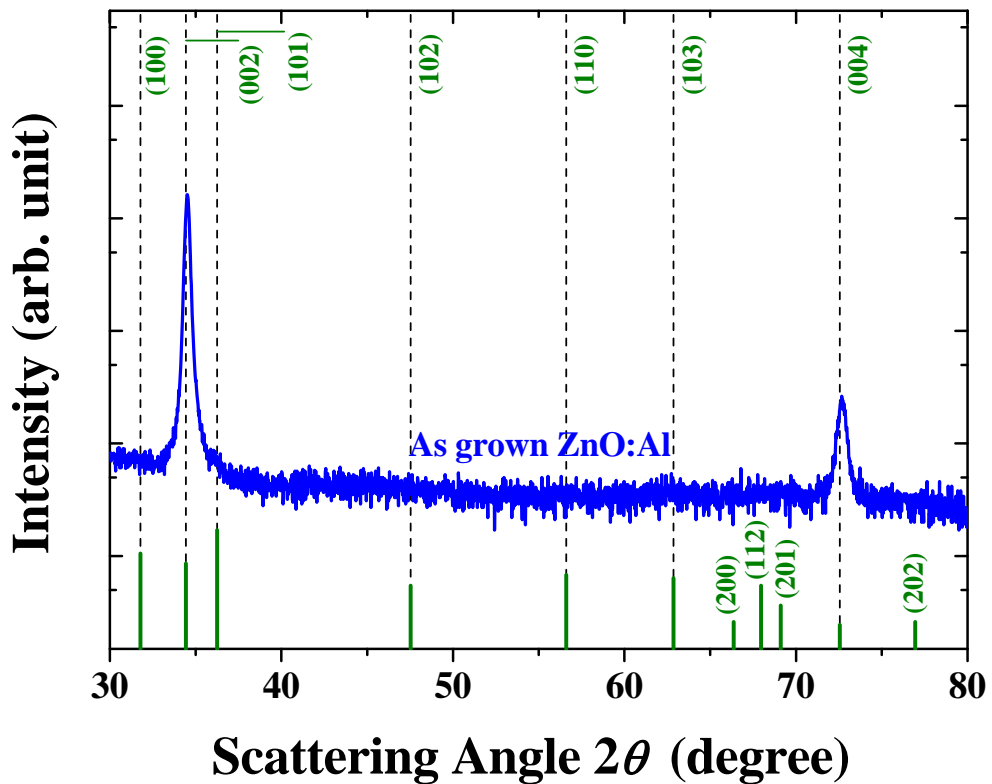


Fig. 2-9. (Color) X-ray diffraction patterns of the ZnO:Al film. The peak intensities and positions from the hexagonal ZnO (JCPDS #36-1451) are shown as solid green bars.

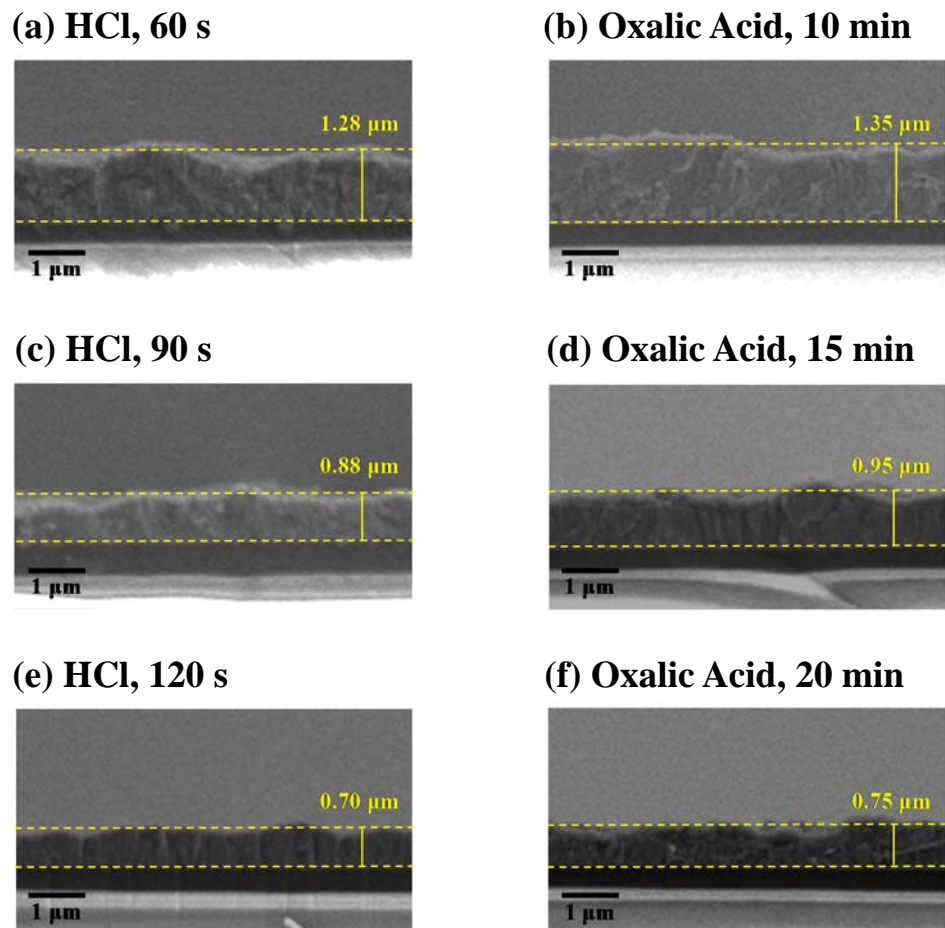


Fig. 2-10. (Color) Cross-sectional SEM images of the textured ZnO:Al films.

(a-c) Etching-time dependence by HCl. (d-f) Etching-time dependence by oxalic acid. Average thickness is denoted for each panel.

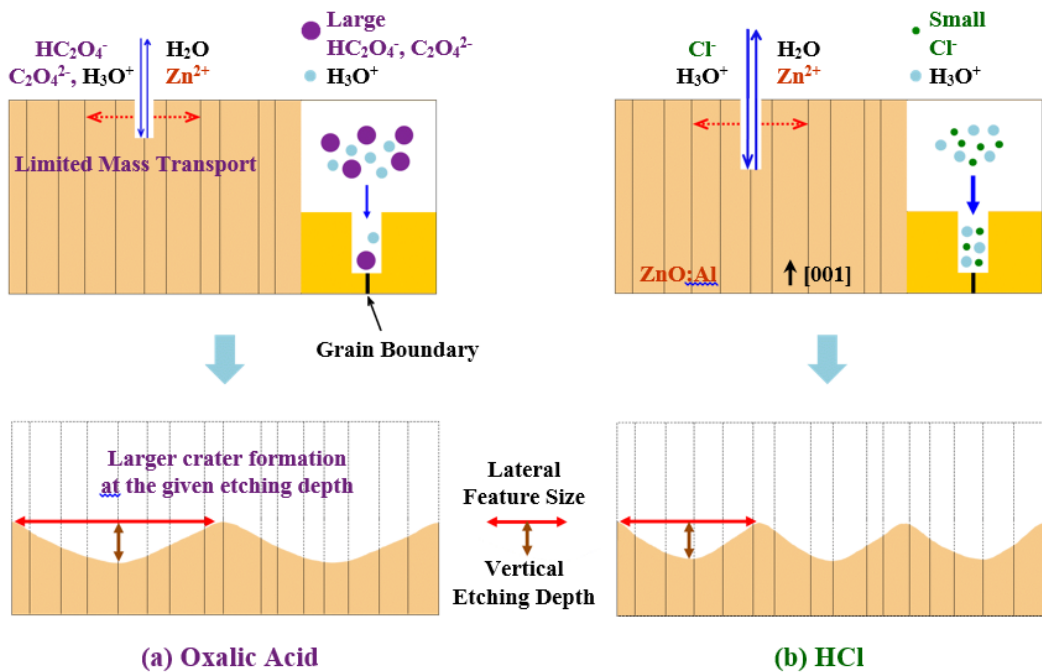


Fig. 2-11. (Color) Etching evolution mechanisms. Schematic illustrations of the phenomenological model, showing the vertical etching through grain boundaries at the initial etching stage (top), and the resultant crater morphologies determined by the competition between vertical etching through the high-angle grain boundaries and lateral etching into the grains (bottom). In case of the oxalic acid, mass transport into grain boundaries is relatively limited due to the larger size of reactants, slowing down the vertical-etching speed compared to that of the lateral etching, which in turn induces larger crater formation at the given etching depth.

In Si thin-film solar cells, oxalic acid, as an alternative to conventional HCl, makes a highly scatterable surface morphology of ZnO:Al, especially at long wavelengths as shown in Fig. 2-12. Without lowering the electrical performance, the increase of optical paths within the absorber layers by multiple scattering can enhance the power-conversion efficiency. We discussed how organic-acid texturing can induce distinctive surface morphology. Parameters for the surface roughness and lateral correlation change with the crater-morphology evolution, and superior light-scattering performance was explained by a haze model describing the interactions between photons and rough interfaces.

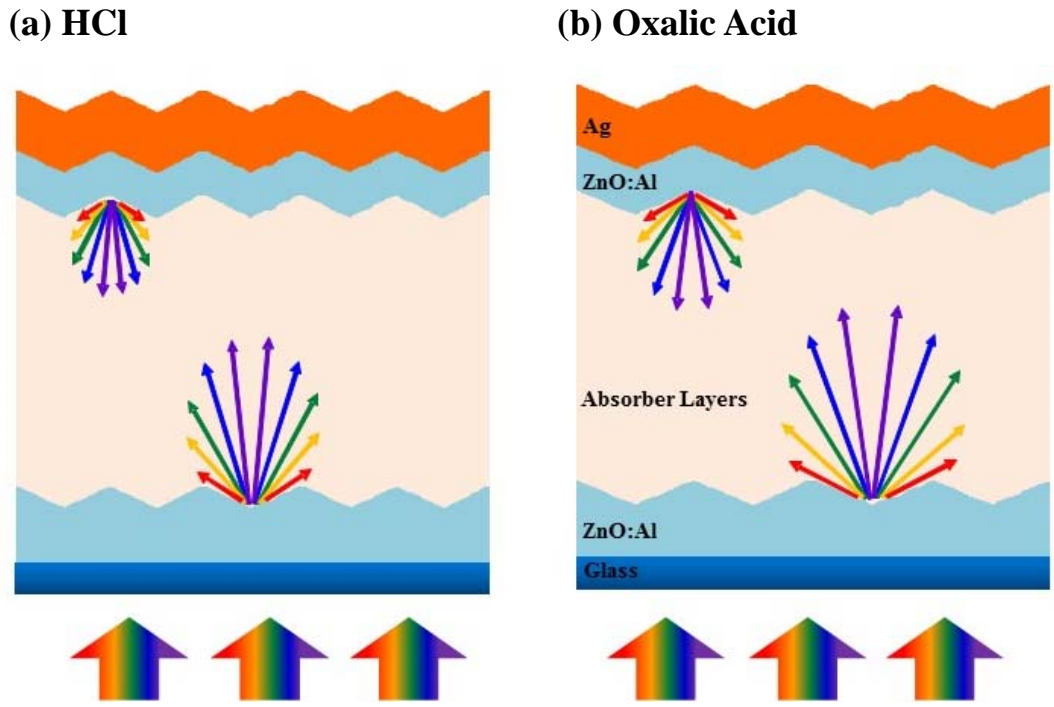


Fig. 2-12. (Color) Schematic illustrations showing light-trapping effects by surface texturing of the front TCOs in Si thin-film solar cells. ZnO:Al textured by (a) HCl and (b) oxalic acid. Relative intensities and wavelengths for scattered lights are represented while the scattering angle is arbitrarily shown.

2.4. Conclusions

The desired morphology for the effective light scattering applicable in thin-film solar cells was facilely obtained by organic-acid etching. The texturing behavior of ZnO:Al by oxalic acid was well characterized by two simple surface parameters: vertical roughness and lateral correlation length. Also, a mass transport model is developed to explain the etching evolution mechanisms. The oxalic-acid texturing exhibited ~8% higher haze value, while maintaining the same transparency and resistance, compared to the HCl etching system. This is straightforwardly explained by using the haze model with the extracted two surface parameters of the textured TCO films. Our results suggest that this novel etching system by oxalic acid broadens strategy spectrum for designing high-efficiency and low-cost thin-film solar cells.

2.5. References

1. B. Shin, O. Gunawan, Y. Zhu, N. Bojarczuk, S. Chey, and S. Guha, “Thin film solar cell with 8.4% power conversion efficiency using an earth-abundant Cu₂ZnSnS₄ absorber,” *Prog. Photovolt. Res. Appl.* **21**, 72 (2013).
2. H. McDaniel, P. Heil, C. Tsai, K. Kim, and M. Shim, “Integration of type II nanorod heterostructures into photovoltaics,” *ACS Nano* **5**, 7677 (2011).
3. D. Kim D, C. Hangarter, R. Debnath , J. Ha, C. Beauchamp, M. Widstrom, J. Guyer, N. Nguyen, B. Yoo, and D. Josell, “Backcontact CdSe/CdTe windowless solar cells,” *Sol. Energ. Mat. Sol. C.* **109**, 246 (2013).
4. G, Kang, H. Park, D. Shin, S. Baek, M. Choi, D. Yu, K. Kim, and W. Padilla, “Broadband light-trapping enhancement in an ultrathin film *a*-Si absorber using whispering gallery modes and guided wave modes with dielectric surface-textured structures,” *Adv. Mater.* **25**, 2617 (2013).
5. J. Grandidier, D. Callchan, J. Munday, and H. Atwater, “Light absorption enhancement in thin-film solar cells using whispering gallery modes in dielectric nanospheres,” *Adv. Mater.* **23**, 1272 (2011).
6. K. Nalwa, J. Park, K. Ho, and S. Chaudhary, “On realizing higher efficiency polymer solar cells using a textured substrate platform,” *Adv. Mater.* **23**, 112 (2011).
7. R. Pala, J. White, E. Barnard, J. Liu, and M. Brongersm, “Design of plasmonic thin-film solar cells with broadband absorption enhancements,” *Adv. Mater.* **21**, 3504 (2009).

8. L. Müller-Meskamp, Y. Kim, T. Roch, S. Hofmann, R. Scholz, S. Echardt, K. Leo, and A. Lasagni, “Efficiency enhancement of organic solar cells by fabricating periodic surface textures using direct laser interference patterning,” *Adv. Mater.* **24**, 906 (2012).
9. C. Hsu, C. Battaglia, C. Pahud, Z. Ruan, F. Haug, S. Fan, C. Ballif, and Y. Cui, “High-efficiency amorphous silicon solar cell on a periodic nanocone back reflector,” *Adv. Mater.* **2**, 628 (2012).
10. X. Sheng, J. Liu, I. Kozinsky, A. Agarwal, J. Michel, and L. Kimerling, “Design and non-lithographic fabrication of light trapping structures for thin film silicon solar cells,” *Adv. Mater.* **23**, 843 (2011).
11. S. Lee, H. Choi, H. Li, K. Ji, S. Nam, J. Choi, S. Ahn, H. Lee H, and B. Park, “Analysis of α -Si:H/TCO contact resistance for the Si heterojunction back-contact solar cell,” *Sol. Energ. Mat. Sol. C.* **120**, 412 (2014).
12. C. Granqvist, “Transparent conductors as solar energy materials: a panoramic review,” *Sol. Energ. Mat. Sol. C.* **91**, 1529 (2007).
13. J. Nomoto, T. Hirano, T. Miyata, and T. Minami, “Preparation of Al-doped ZnO transparent electrodes suitable for thin-film solar cell applications by various types of magnetron sputtering depositions,” *Thin Solid Films* **520**, 1400 (2011).
14. J. Müller, B. Rech, J. Springer, and M. Vanecek, “TCO and light trapping in silicon thin film solar cells,” *Sol. Energ. Mat. Sol. C.* **77**, 917 (2004)
15. O. Kluth, G. Schöpe, J. Hüpkes, C. Agashe, J. Müller, and B. Rech, “Modified Thornton model for magnetron sputtered zinc oxide: film structure and etching behaviour,” *Thin Solid Films* **442**, 80 (2003).

16. T. Moon, W. Yoon, K. Ji, S. Ahn, S. Lee, M. Joo, H. Shin, K. Park, and H. Lee, "Microstructure and light-scattering properties of ZnO:Al films prepared using a two-step process through the control of oxygen pressure," *Appl. Phys. Express* **3**, 095801 (2012).
17. Y. Zhao, S. Miyajima, Y. Ide, A. Yamada, and M. Konagai, "Microcrystalline silicon films and solar cells prepared by photochemical vapor deposition on textured SnO₂ with high haze factors," *J. Jpn. Appl. Phys.* **41**, 6417 (2002).
18. M. Berginski, J. Hüpkes, M. Schulte, G. Schöpe, H. Stiebig, and B. Rech, "The effect of front ZnO:Al surface texture and optical transparency on efficient light trapping in silicon thin-film solar cells," *J. Appl. Phys.* **101**, 074903 (2002).
19. S. Fernandez, O. Abril, F. Naranjo, and J. Gandia, "Amorphous and nanocrystalline silicon growth on carbon nanotube substrates," *Thin Solid Films* **520**, 4144 (2011).
20. Y. Lin, B. Wang, W. Yen, and C. Shen, "Surface textured molybdenum doped zinc oxide thin films prepared for thin film solar cells using pulsed direct current magnetron sputtering," *Thin Solid Films* **519**, 5571 (2011).
21. H. Zhu, J. Hüpkes, E. Bunte, J. Owen, and S. Huang, "Novel etching method on high rate ZnO:Al thin films reactively sputtered from dual tube metallic targets for silicon-based solar cells," *Sol. Energ. Mat. Sol. C.* **95**, 964 (2011).
22. D. Lee, J. Kwon, Y. Lim, and H. Yang, "Concentration-dependent wet etching behaviors of Ga-doped ZnO films sputter-deposited at room temperature using formic and citric acids," *J. Electrochem. Soc.* **157**, D428 (2010).

23. J. Hüpkes, J. Owen, S. Pust, and E. Bunte, “Chemical etching of zinc oxide for thin-film silicon solar cells,” *ChemPhysChem* **13**, 66 (2012).
24. C. Lin, W Liu, and C. Hsieh, “Scalar scattering model of highly textured transparent conducting oxide,” *J. Appl. Phys.* **109** 014508 (2011).
25. P. Bechmann, and A. Spizzichino, “The scattering of electromagnetic waves from rough surfaces,” *Pergamon Press* p 48, 1963.
26. J. Porteus, “Relation between the height distribution of a rough surface and the reflectance at normal incidence,” *J. Opt. Soc. Am.* **53**, 1394 (1963).
27. I. Simonsen, A. Larsen, E. Andreassen, E. Ommundsen, and K. Norvdvarhaug, “Haze of surface random systems: an approximate analytic approach,” *Phys. Rev. A* **79**, 063813 (2009).
28. D. Lee, S. Lee, J. Bang, H. Yang, “Wet chemical etching of transparent conducting Ga-doped ZnO thin films by oxalic and formic acid,” *J. Electrochem. Soc.* **156**, D211 (2009).
29. P. Washington, H. Ong, J. Dai, R. Chang, “Determination of the optical constants of zinc oxide thin films by spectroscopic ellipsometry,” *Appl. Phys. Lett.* **72**, 3261 (1998).
30. J. Hupkes, J. Owen, S. Pust, and E. Bunte, “Chemical etching of zinc oxide for thin-film silicon solar cells,” *ChemPhysChem* **13**, 66 (2012).
31. Q. Jinag, J. Lu, J. Zhang, Y. Yuan, H. Cai, C. Wu, R. Sun, B. Lu, X. Pan, and Z. Ye, “Texture surfaces and etching mechanism of ZnO:Al films by a neutral agent for solar cells,” *Sol. Energ. Mat. Sol. C* **130**, 264 (2014).

Chapter 3.

Summary

In this thesis, an organic acid for the surface texturing of ZnO:Al is investigated as an alternative to conventional HCl etching. The texturing behavior by oxalic acid was explained in terms of vertical roughness, lateral correlation length, and thickness change with the crater evolution. The enhancement of light scattering by oxalic acid was demonstrated without any deterioration of transparency or resistance.

The round-shape interface formed by oxalic acid would be helpful for the quality of semiconductor absorber layers by minimizing defective region formed during the oriented-growth collision, suppressing charge-carrier recombination. Nowadays, many researchers have reported about complicated photonic or plasmonic metallic structures for efficient light trapping methods. However, despite the successful applications in laboratory scale, manufacturability is questionable due to concerns with cost and reproducibility. The organic-acid texturing proposed in this study can offer manufacturing-compatible tunability for the desirable TCO-texturing morphology, broadening the strategy spectrum for the design of solar cells in industry. Significantly, deeper understanding about the correlation between etching characteristics and texturing morphologies can give keen insight for the suitable direction of TCO development.

Appendix 1.

***Facile Converstion Synthesis of Densely-Formed Branched ZnO Nanowire Arrays for Quantum-Dot-Sensitized Solar Cells**

A.1.1. Introduction

The rational design and synthesis of semiconducting nanowire building blocks with well-defined structures and compositions are the central tasks for the fabrication of nanoelectronic and photovoltaic devices [1-5]. Compared to the simple one-dimensional (1-D) nanostructures, sophisticated three-dimensional (3-D) nanostructures, like branches grown on the nanowire backbones, are considered as a promising structure for the nanoscale building blocks in the aspects of an increased surface area for light absorption and sensitizers, as well as efficient channels for the photogenerated electron transports [6-9].

Especially, ZnO with multidimensional structures for photovoltaic devices have been intensively investigated owing to its relatively easy synthesis and higher

*The work presented in Appendix 1 was published in *Electrochim. Acta* entitled,

“Facile Conversion Synthesis of Densely-Formed BranchedZnO-Nanowire Arrays for Quantum-Dot-Sensitized Solar Cells,”

Woojin Lee, Suji Kang, Taehyun Hwang, Kunsu Kim, Hyungsub Woo, Byungho Lee, Jaewon Kim, Jinhyun Kim, and Byungwoo Park.*

electron mobility than TiO₂. Many research groups have synthesized branched ZnO nanowires with the expectations to obtain high power conversion efficiency (PCE) of semiconductor-sensitized solar cells (SSCs) [10-12]. Cheng *et al.* and Ko *et al.* have shown that branched treelike hierarchical ZnO photoelectrodes prepared via a two-step solvothermal growth have enhanced the PCE of dye-sensitized solar cells (DSSCs) [11,12]. However, the synthesized 3-D ZnO nanostructures have suffered from incomplete coverage of branches on the nanowire backbones, leading to the insufficient surface area, which resulted in the limited sensitizer-loading capacity [13-15].

In this work, densely-formed branched ZnO-nanowire architectures were prepared by combining a straightforward conversion reaction and hydrothermal growth for the quantum-dot sensitized solar cells (QDSCs). The factor-of-two enhancement by branching is systematically correlated with the light harvesting efficiency, charge-transfer resistance, and carrier lifetime. This simple and controllable branch growth for the hierarchical nanostructures provides an advanced insight into the design of photoanode with more effective light harvesting and charge collection.

A.1.2. Experimental Section

A.1.2.1. Synthesis of 1-D Nanostructures

Fluorine-doped tin oxide substrates (FTO, TEC 8: Pilkington) were served as substrates. For the TiO₂ blocking layer, pure TiCl₄ was added to pre-cooled (~0°C) deionized H₂O to make a 40 mM TiCl₄ aqueous solution, and the substrates were dipped in the solution for 30 min at 70°C, followed by annealing at 450°C for 30 min under air. For hydrothermal ZnO-nanowire growth, the Gao group's method was adopted [5]. First, ZnO seeds were grown on the TiCl₄-treated FTO, for which 0.5 mM zinc acetate dihydrate (Zn(CH₃COO)₂ 2H₂O) ethanol solution of 50 μL was dropped on the substrate, spin-coated at 3000 rpm for 30 s, and subsequently dried on a hot plate at 60°C. This procedure was repeated for 5 times, and finally the zinc acetate dihydrate was thermally decomposed by annealing under air at 400°C for 1 h to make ZnO. The seeded substrates were immersed in the aqueous solutions consisting of 25 mM of zinc nitrate hexahydrate, 25 mM of hexamethylenetetramine (HMTA), ammonium hydroxide (NH₄OH), and 3.5 mM poly(ethyleneimine) (PEI) in autoclaves. Hydrothermal syntheses were carried out at 95°C for 8 h in the preheated oven. After the hydrothermal reaction, the ZnO-nanowire grown substrates were rinsed with ethanol and then dried at 60°C. To remove any organic residues, heat treatments at 450°C for 1 h under air were conducted.

A.1.2.2. Branched ZnO Nanowire Growth

The pristine ZnO nanowires substrates were firstly immersed into 4 mM Na₂S aqueous solution for 0 - 24 h. Then, the substrates were rinsed with deionized water for several times to remove the residual Na₂S and then dried. These substrates were further annealed at 500°C for 3h in air to convert the ZnS into ZnO. Subsequently, the annealed samples were used as substrates for the second hydrothermal growth of ZnO nanowires under the same experimental conditions (with the 3-h annealing at 95°C). Finally, all the samples were annealed at 450°C for 1 h to remove any possible organic residues.

A.1.2.3. Device Fabrication

In order to improve the solar cell efficiency, the as-prepared samples were immersed in 20 mM titanium butoxide (Ti[O(CH₂)₃CH]₄: Aldrich) in 2-propanol at room temperature, and the films were post-annealed at 450°C for 30 min. The CdS quantum dots were coated on the branched ZnO nanowires by a successive ionic-layer adsorption and reaction (SILAR) [16] with 14-repeated cycles. Polysulfide electrolyte was prepared by dissolving 0.5 M Na₂S, 1 M S, and 0.02 M KCl in methanol/water solutions (7/3 volumetric ratio) [17]. For a counter electrode, Ti was deposited on the pre-drilled FTO substrates as adhesion layer, and Cu was deposited by rf magnetron sputtering. The Cu-deposited films were

sulfurized in a polysulfide solution [18], and thermoplastic foil (60 μm ; Dupont) was used as a spacer.

A.1.2.3. Characterization

For the morphology evolution of the branched ZnO nanowires, field-emission scanning electron microscopy (FE-SEM, JSM-6330F: JEOL) was used. X-ray diffraction (XRD, M18XHF-SRA: Mac Science) was carried out for the analyses of the crystalline phases. The photocurrent-voltage (J-V) curves were measured by the solar cell measurement system (K3000: McScience) with the solar simulator (Xenon lamp, air mass (AM 1.5, 100 mW/cm²). The absorptance and diffused reflectance were recorded by a UV/Vis spectrophotometer (Cary 5000: Agilent Technologies). An inductively coupled plasma-atomic emission spectrometer (ICP-AES, Optima-4300 DV: Perkin-Elmer) was used to measure the amount of Cd atoms loaded onto the ZnO-branched electrode. An incident photon-to-current conversion efficiency (IPCE) measurement system (K3100: McScience) was used to obtain the external quantum efficiency, and the electrochemical impedance and open-circuit voltage decay were obtained from a potentiostat (CHI 608C: CH Instrumental Inc.).

A.1.3. Results and Discussion

Figure A1-1 shows the strategies for the densely-formed branched ZnO-nanowire photoelectrode. Vertically oriented ZnO trunks (backbones) were grown on the seeded FTO substrate through a hydrothermal method. In order to grow a uniform secondary branching, ZnO seed layers are required [26,27]. By a straightforward ion-exchange reaction of ZnS into ZnO, highly-packed ZnO seeds are obtained by calcinating ZnS-nanoparticle shells in air, thereby utilizing compact ZnO-nanowire branches by the additional hydrothermal process. After passivation of any residual defects, the optimized photoelectrodes are achieved with the improved carrier lifetime.

From the SEM images (Fig. A1-2), the pristine ZnO nanowires are grown vertically well on the FTO substrate with thicknesses up to 10 μm and diameters ranging from 100 to 300 nm. For the secondary-grown nanobranches, the nanobranch lengths are in the range of 1 to 2 μm with diameters of 30 - 50 nm. The hierarchical nanowire structures are clearly observed with the samples over 1-h thioacetamide (TAA) treatment (Figs. A1-2(b)-(d)).

For the effects of 3-D branched morphologies on the light scattering, Fig. A1-3(a) shows the absorptance and diffused reflectance at various conditions. The branched nanowires exhibit higher diffused reflectance (400 - 800 nm), confirming higher absorptance by the ZnO branches, due to the increased optical-path lengths

[28,29]. The diffused transmittance with CdS sensitization was measured (Fig. A1-3 (b)) indicating better light-harvesting efficiency (through $A = 1 - R - T$ where A , R , and T are absorptance, diffused reflectance, and diffused transmittance, respectively [30]).

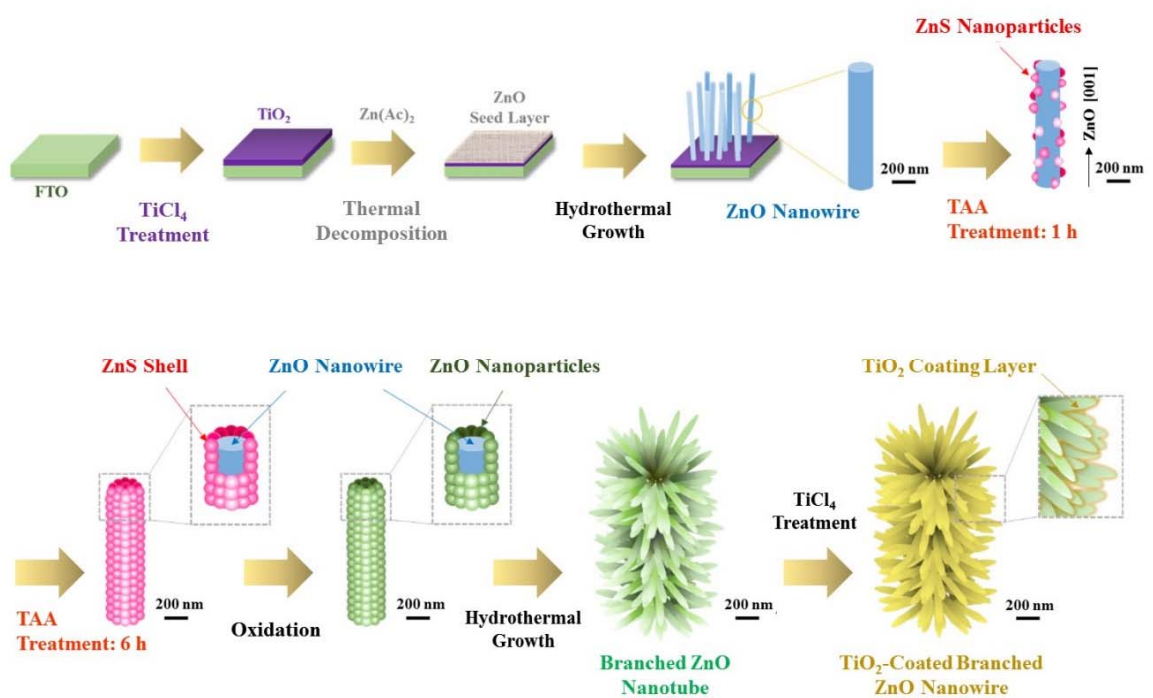


Fig. A1-1. (Color) Schematic illustration of the nanostructural evolution in 3-dimensional hierarchical ZnO nanowires with various treatments.

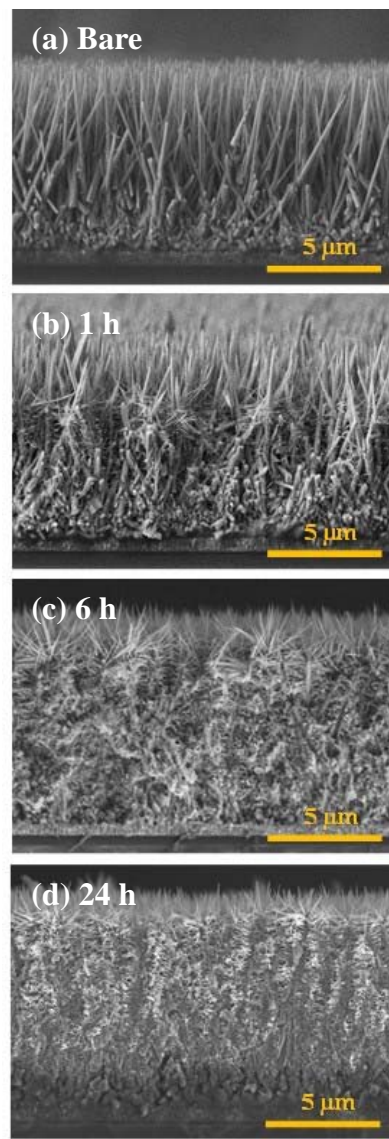


Fig. A1-2. (Color) Cross-sectional SEM of densely-formed branches ZnO nanowire arrays with various TAA (thioacetamide) treatments: (a) No treatment (bare), (b) 1-h, (c) 6-h, and (d) 24-h TAA treatments.

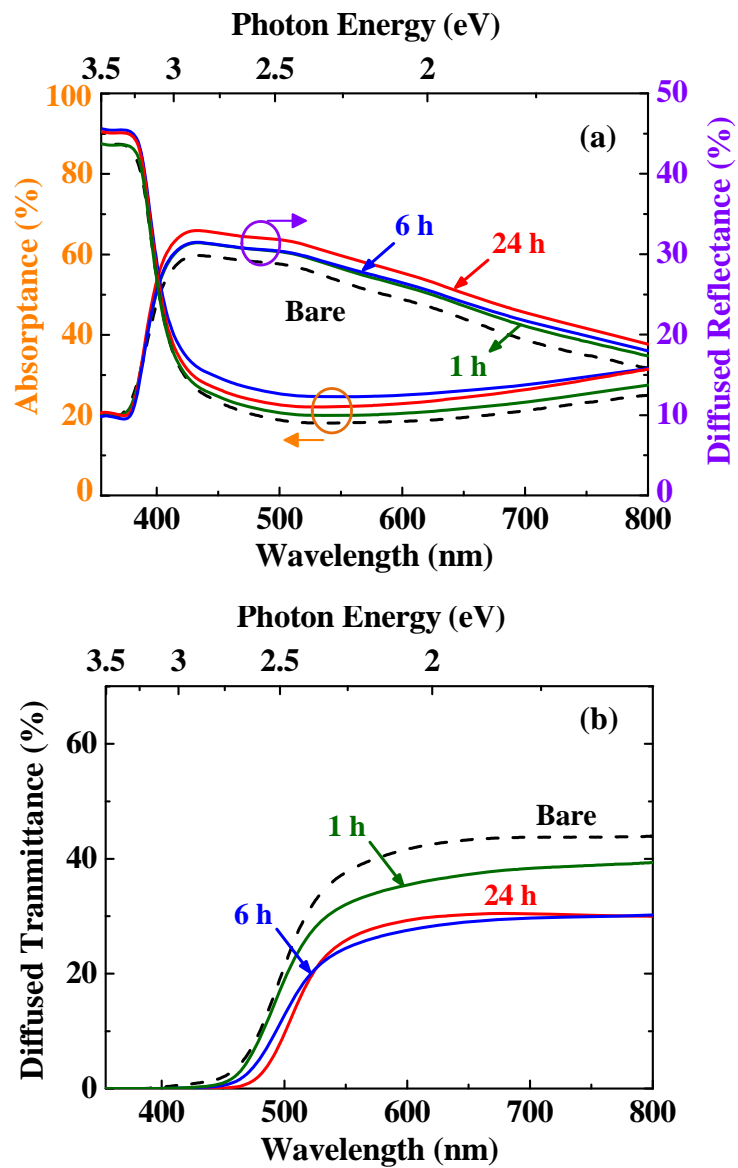


Fig. A1-3. (Color) Optical properties of hierarchical ZnO nanostructures at various TAA treatment times: (a) Absorptance and diffused reflectance spectra before CdS sensitization. (b) Diffused transmittance spectra after CdS sensitization.

A quantitative analysis by ICP-AES also revealed that the amount of CdS quantum dots is increased by branching. The Cd/Sn atomic ratios stood at 8.0, 12.2, 14.4, and 15.7, respectively, for the bare, 1-h, 6-h, and 24-h treated ZnO hierarchical structures, though the Cd/Zn ratios were the same in all the samples (Table AI). Especially, the Cd atoms loaded on the 6-h-treated sample increased by ~80% compared to the bare photoanode.

The effects of the TAA treatments were systematically investigated through SEM, TEM, and XRD (Fig. A1-4 – A1-7). After the ion-exchange reaction in Na₂S solution for 6 h (TAA treatment), ZnS nanoparticles are formed on the ZnO nanowire backbones (lattice spacing of 0.31 nm for ZnS (111) planes in Fig. A1-4(b) [31]). For the ZnO/ZnO nanowire/nanoparticle formation, the HRTEM images (Fig. A1-4(c)) exhibit many ZnO nanoparticles on the surface of the nanowires (with the lattice spacing of 0.26 and 0.28 nm, respectively, for the ZnO (002) and (100) planes [32,33]). Then, after the hydrothermal process, hierarchically branched ZnO nanowire arrays are successfully synthesized (Fig. A1-4(d)). Both the branches and backbones are single-crystalline nanowires along the [001] growth directions.

During the each synthesis procedure, the diffraction data exhibit wurtzite ZnO crystalline structure (JCPDS #36-1451) with no impurity peaks. Overall, the strong (002) peaks indicate that the backbone nanowires are oriented more into the

c-axis direction [34]. After an ion-exchange reaction, a broader diffraction peak located at 28.8° is due to the ZnS (111) peak (JCPDS #05-0566) from the ZnO-core (nanowire) / ZnS-shell (nanoparticle) arrays. It is also worthwhile to notice that the branched nanowire arrays show stronger ZnO (100) peak consistently.

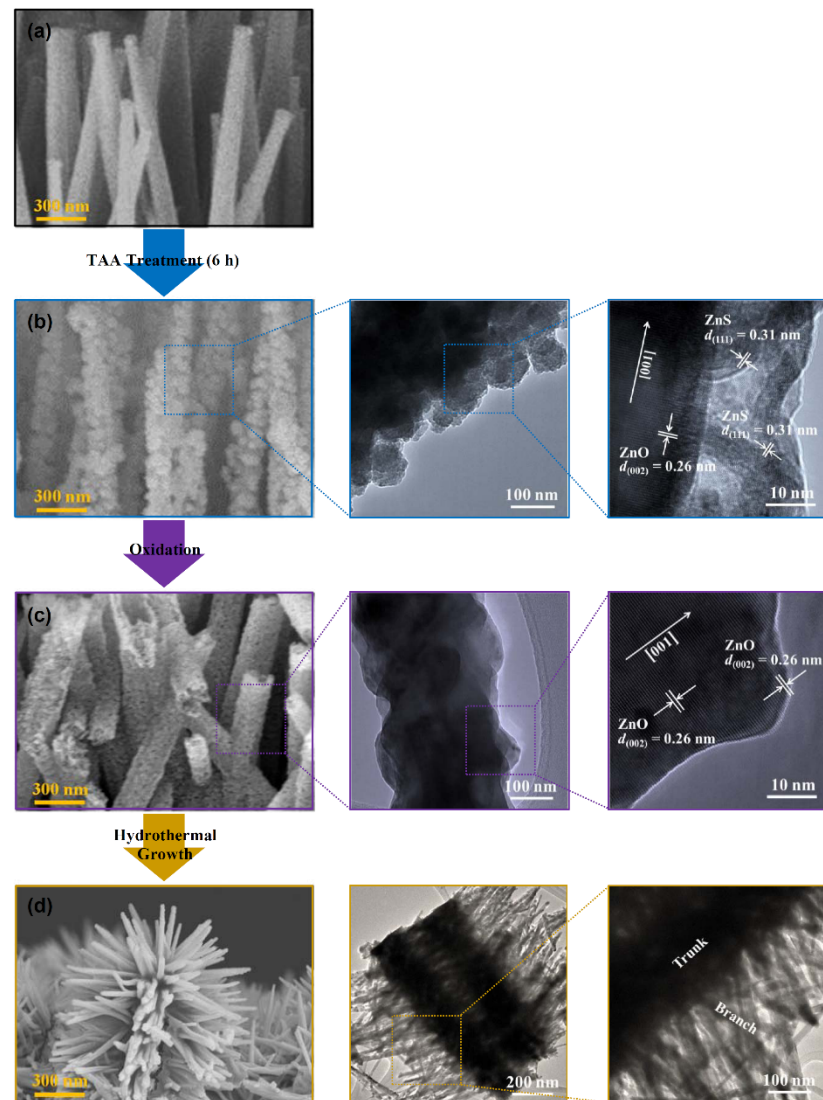


Fig. A1-4. (Color) Typical SEM and TEM images of ZnO nanostructures during each synthesis procedure (with 6-h TAA treatment time): (a) Bare, (b) ZnO/ZnS core/shell nanowires, (c) ZnO/ZnO core/nanoparticle nanowires, and (d) Branched ZnO.

Table AI. Atomic ratios measured from the ICP results of CdS sensitizers with various TAA treatment times.

Cell	Cd/Sn	Zn/Sn	Cd/Zn
Bare	8.0	88	0.091
1 h	12.2	139	0.088
6 h	14.4	159	0.092
24 h	15.7	170	0.091

* Cd from the CdS sensitizer, Sn from the FTO substrates, and Zn from the ZnO hierarchical structures.

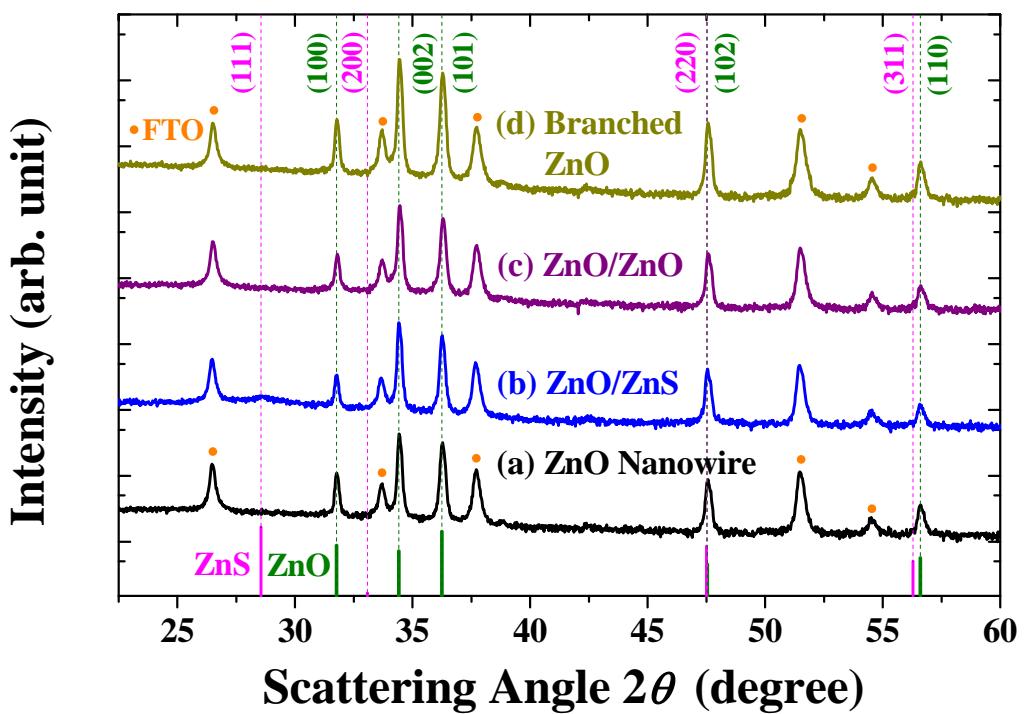


Fig. A1-5. (Color) X-ray diffraction of the nanostructures showing the crystalline-phase evolution.

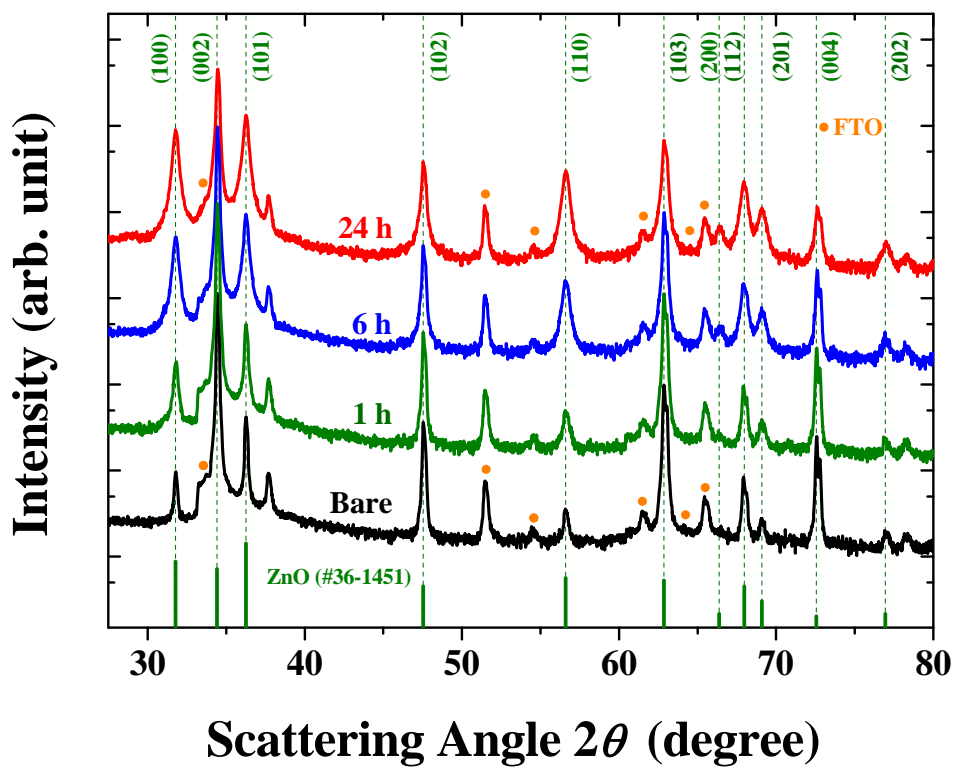


Fig. A1-6. (Color) X-ray diffraction of 3-D branched ZnO nanostructures with various TAA treatment times (after oxidation of ZnS shell and hydrothermal growth of ZnO branches).

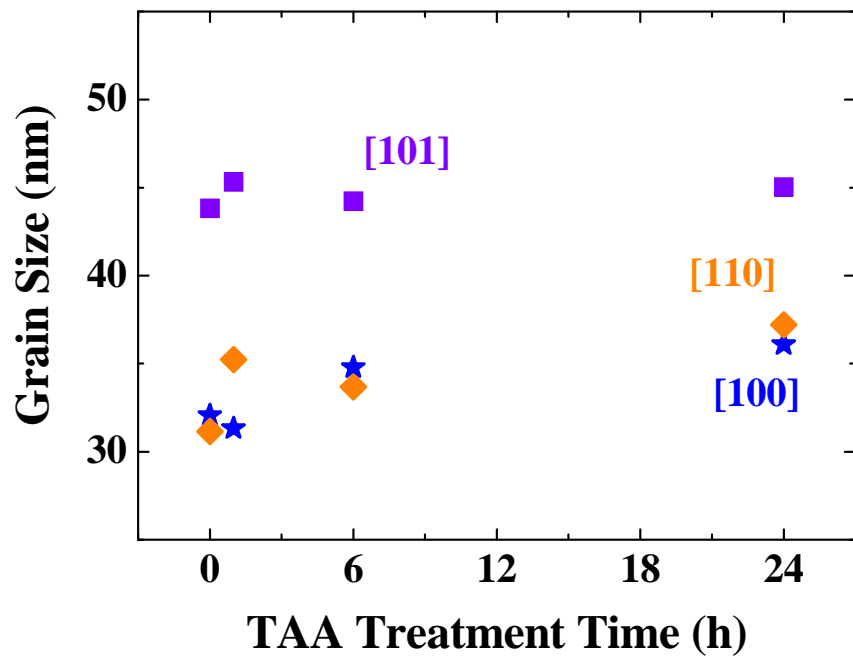


Fig. A1-7. (Color) Grain size of ZnO along the $[hkl]$ directions as a function of TAA treatment time.

For the fabrication of QDSCs with the densely-formed branched nanostructures, the crystallinity of arrays was confirmed by XRD (Fig. A1-6) with the grain-size evolution (Fig. A1-7). The sharper (hkl) peaks for the branched ZnO arrays were observed as the TAA treatment time increased, indicating relative easy grain growths with the increase of the branch densities [14,35]. The photocurrent-voltage curves of the QDSCs under AM 1.5 illumination, shown in Fig. A1-8, show the improved short-circuit current with the increase of TAA treatment, which is consistent with the diffused transmission (Fig. A1-3(b)) and ICP results (Table AI). Accordingly, the power-conversion efficiencies are also enhanced (Table AII). In contrast, the 24-h treated sample exhibits lower efficiency, which is caused by both the reduced diffusivity of polysulfide electrolyte [36] and increased reflectance due to the less porous nanostructure [37].

Due to the various types of defects at the surface of ZnO nanowire arrays, such as oxygen vacancies, zinc vacancies, oxygen atoms at the zinc position in the crystal lattice, donor-acceptor pair, etc. [38,39], the enlarged surface area of the 3-D ZnO nanostructures provides more charge recombination sites with S^- in the electrolyte. Therefore, surface passivation by TiO₂ was conducted to suppress possible charge recombination. As expected, the TiO₂ coating enhanced both the short-circuit current and power-conversion efficiency of QDSC by ~20%, as shown in Fig. A1-8 and Table AII.

The incident photon to current conversion efficiency (IPCE) at wavelength λ is expressed as [40]:

$$\text{IPCE}(\lambda) = \text{LHE}(\lambda) \varphi_{inj} \eta_{cc}, \quad (1)$$

where LHE (λ), φ_{inj} , and η_{cc} are the light-harvesting efficiency, the electron injection quantum yield from QDs to photoelectrode, and charge collection efficiency, respectively. The TiO₂-coated sample shows the higher IPCE value (Fig. A1-9) with comparable amount of QDs (Fig. A1-12), revealing that the increased photocurrent after the TiO₂ coating results from the enhancement of both η_{cc} and φ_{inj} [40].

The recombination rate at the ZnO / polysulfide electrolyte interface was confirmed by the impedance analysis (Fig. A1-10). By fitting the Nyquist and Bode plots based on the equivalent-circuit model, the recombination resistance improved with the TiO₂ coating from 185 ± 2 to $212 \pm 2 \Omega$ (Table AIII). It can be explained by the existence of additional thin TiO₂-coating layer, which passivates charge-trapping sites on the nanowire surface and also enhances the connectivity between branches and nanowire backbones.

For the further investigation of carrier recombination, the open-circuit voltage decay (OCVD) measurements were performed, as shown in Fig. A1-11. From the OCVD curves, the carrier lifetime (τ) can be obtained as [41-43]:

$$\tau = -\frac{k_B T}{e} \left(\frac{dV_{oc}}{dt} \right)^{-1} \quad (2)$$

where k_B , e , and T are the Boltzmann's constant, the electric charge, and the temperature, respectively. The TiO₂-coated sample exhibits a higher carrier lifetime compared with the bare sample (the inset of Fig. A1-11). This result also supports the TiO₂-passivation effects on the ZnO nanostructures. It is interesting to observe the slower decay response of the QDSCs with branched structures compared to the bare ZnO one. We cautiously consider that it may be caused by the core / shell nature of branched nanostructures [44,45], but it needs further investigation.

Table AII. Photovoltaic performance of the QDSCs. Short-circuit current density (J_{sc}), open-circuit voltage (V_{oc}), fill factor (FF), and power-conversion efficiency (η) of the QDSCs with various TAA treatment times.

Cell	J_{sc} (mA cm ⁻²)	V_{oc} (V)	FF	η
Bare	3.82	0.59	0.33	0.74%
1 h	4.50	0.61	0.33	0.91%
6 h	5.88	0.60	0.34	1.19%
24 h	5.76	0.56	0.33	1.08%
6 h + TiO₂	6.95	0.61	0.34	1.43%

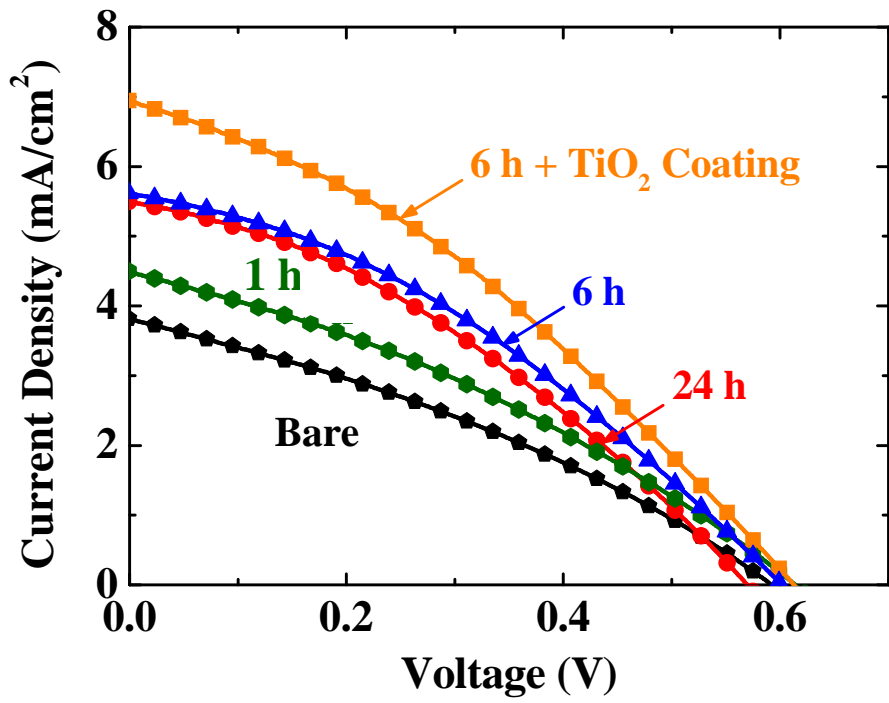


Fig. A1-8. (Color) Photocurrent-voltage curves of the QDSCs based on the nanostructured photoanodes with different TAA treatment times.

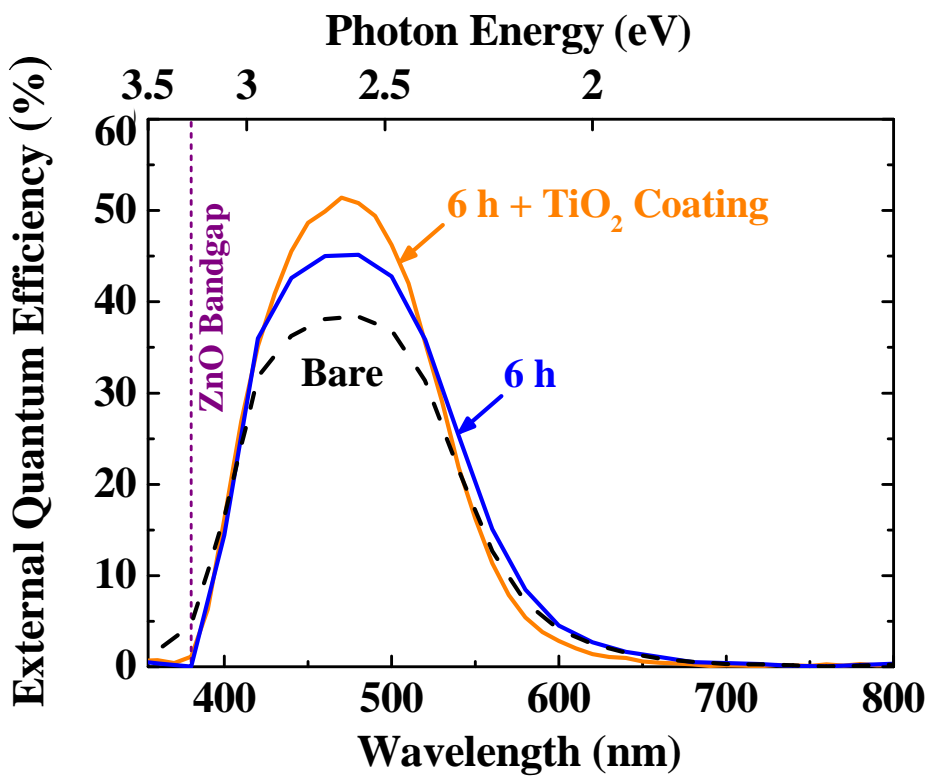


Fig. A1-9. (Color) Incident photon-to-current conversion efficiency (IPCE) spectra.

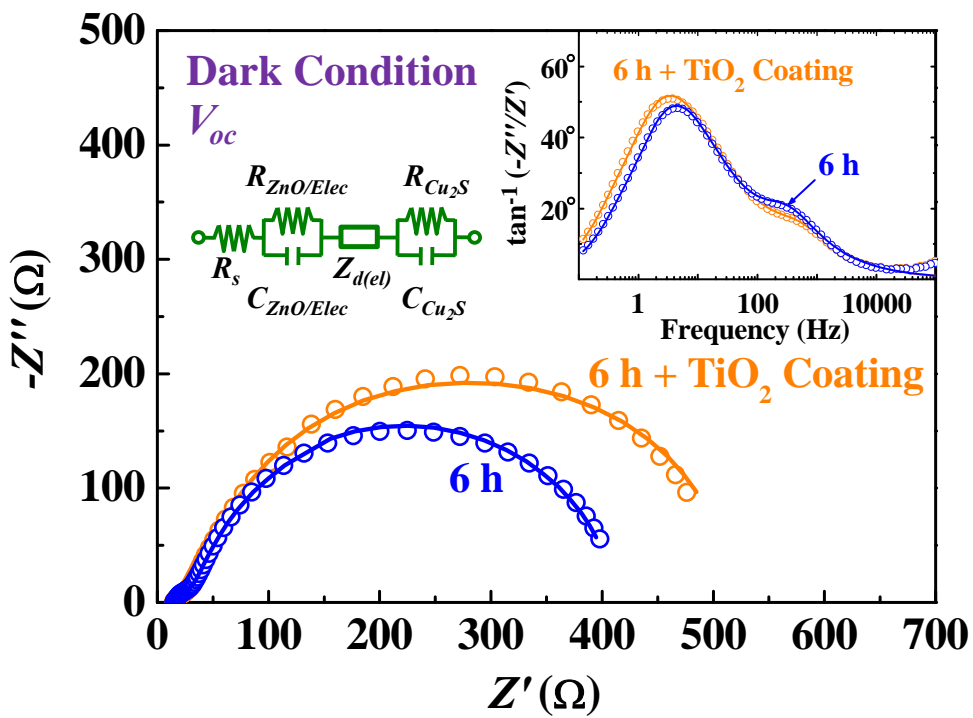


Fig. A1-10. (Color) Electrochemical impedance spectra of Nyquist plot for the QDSCs (6 h of TAA treatment time) with and without TiO₂ treatment. The inset exhibits the Bode plots. Solid lines are the fitting results using the equivalent circuit model in the inset.

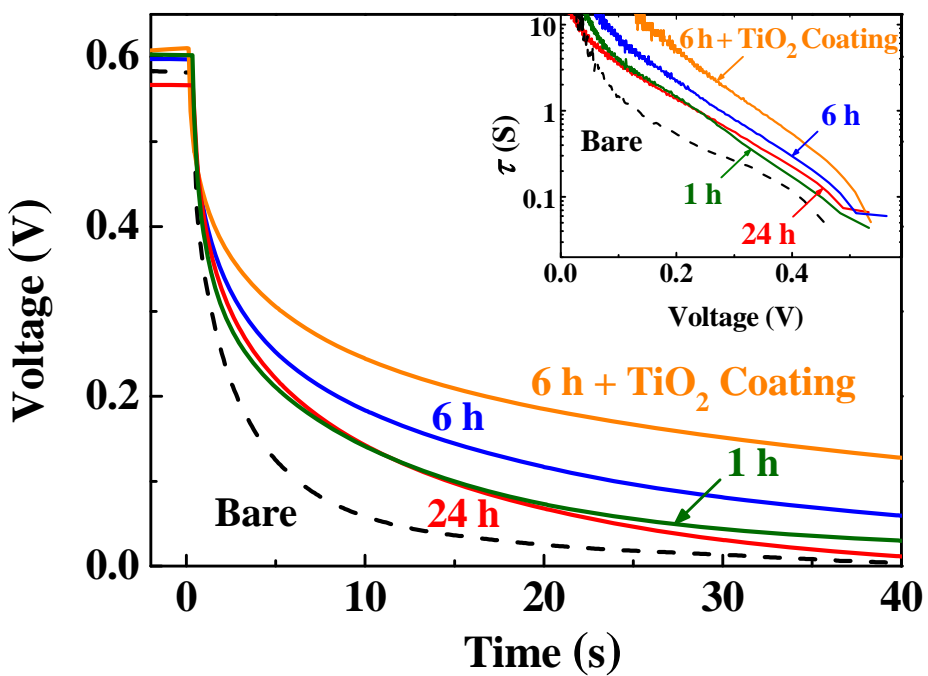


Fig. A1-11. (Color) Experimental decay curves of V_{oc} for the QDSCs. The inset shows the corresponding electron lifetimes.

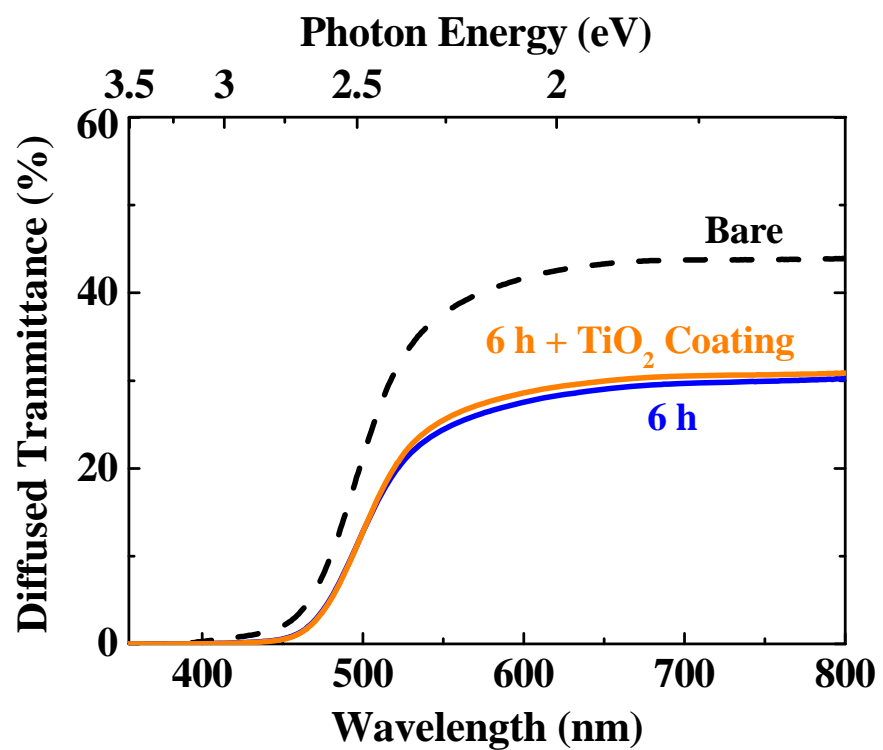
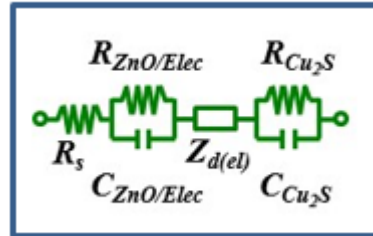


Fig. A1-12. (Color) Diffused transmittance spectra after the CdS sensitization for the QDSCs (6-h TAA treatment), with and without TiO₂ treatment.

Table AIII. Impedance parameters extracted using the equivalent-circuit model for QDSCs.



Parameter	TAA 6 h	6 h + TiO ₂ Coating
R_s (Ω)	15.1 ± 0.1	17.5 ± 0.1
R_{Cu_2S} (Ω)	10.3	10.3
C_{Cu_2S} (μF)	61.0	61.0
$R_{ZnO/Elec}$ (Ω)	185 ± 2	212 ± 2
$C_{ZnO/Elec}$ (μF)	534 ± 4	429 ± 4
$Z_{d(el)}\text{-}R$ (Ω)	197 ± 1	210 ± 1
$Z_{d(el)}\text{-}T$ (ms)	859 ± 3	827 ± 3
$Z_{d(el)}\text{-}P$	0.50	0.50

* The impedance parameters are obtained through fitting while the $Z_{d(el)}\text{-}P$, R_{Cu_2S} , and C_{Cu_2S} values are fixed from the average.

$$Z = R_s + \left[\frac{R_{ZnO/Elec}}{1 + (i\omega)R_{ZnO/Elec}C_{ZnO/Elec}} \right] + \left[R_{ZnO/Elec} \frac{\tanh(i\omega T)^P}{(i\omega T)^P} \right] + \left[\frac{R_{Cu_2S}}{1 + (i\omega)R_{Cu_2S}C_{Cu_2S}} \right]$$

R_s : Series resistance of FTO

$R_{ZnO/Elec}$: Recombination resistance of ZnO/electrolyte interface

$C_{ZnO/Elec}$: Capacitance of ZnO/electrolyte interface

$Z_{d(el)}(R, T, P)$: Warburg impedance of electrolyte diffusion

R : Diffusion resistance, T : Reciprocal of characteristic frequency, $P = 0.5$

R_{Cu_2S} : Charge-transfer resistance of Cu₂S/electrolyte interface

C_{Cu_2S} : Capacitance of Cu₂S/electrolyte interface

A.1.4. Conclusion

Three-dimension hierarchically branched ZnO-nanowire arrays were straightforwardly synthesized with proper nucleation seed layers for the effective branch growth. The resulting densely-formed branched ZnO-nanowire-array photoelectrodes showed enhanced PCE by a factor of two compared to the bare ZnO nanowires, by taking advantages of the light harvesting efficiency, charge-transfer resistance, and carrier lifetime. This easily controllable branching synthesis can be applicable to other photoelectrodes to improve the efficiencies of light harvesting and carrier collection.

A.1.5. References

1. D. Caselli, Z. Liu, D. Shelhammer, and C.-Z. Ning, “Composition-Graded Nanowire Solar Cells Fabricated in a Single Process for Spectrum-Splitting Photovoltaic Systems”, *Nano Lett.* 14 (2014) 5772.
2. C. Xie, B. Nie, L. Zeng, F.-X. Liang, M.-Z. Wang, L. Luo, M. Feng, Y. Yu, C.-Y. Wu, Y. Wu, and S.-H. Yu, “Core-Shell Heterojunction of Silicon Nanowire Arrays and Carbon Quantum Dots for Photovoltaic Devices and Self-Driven Photodetectors”, *ACS Nano* 8 (2014) 4015.
3. W.-Q. Wu, H.-L. Feng, H.-S. Rao, D.-B. Kuang, and C.-Y. Su, “Rational Surface Engineering of Anatase Titania Core-Shell Nanowire Arrays: Full-Solution Processed Synthesis and Remarkable Photovoltaic Performance”, *ACS Appl. Mat. Inter.* 6 (2014) 19100.
4. Z. Peng, Y. Liu, Y. Zhao, K. Chen, Y. Cheng, and W. Chen, “Incorporation of the TiO₂ Nanowire Arrays Counter Electrodes on the Photovoltaic Performance of Quantum Dot Sensitized Solar Cells”, *Electrochim. Acta* 135 (2014) 276.
5. H. Kim and K. Yong, “A Highly Efficient Light Capturing 2D (Nanosheet)-1D (Nanorod) Combined Hierarchical ZnO Nanostructure for Efficient Quantum Dot Sensitized Solar Cells”, *Phys. Chem. Chem. Phys.* 15 (2013) 2109.
6. D. Josell, R. Debnath, J. Ha, J. Guyer, M. Sahiner, C. Reehil, W. Manners, and N. Nguyen, “Windowless CdSe/CdTe Solar Cells with Differentiated Back Contacts: J-V, EQE, and Photocurrent Mapping”, *ACS Appl. Mater. Inter.* 6

(2014) 15972.

7. Y.-G. Lin, Y.-K. Hsu, Y.-C. Chen, B.-W. Lee, J.-S. Hwang, L.-C. Chen, and K.-H. Chen, “Cobalt-Phosphate-Assisted Photoelectrochemical Water Oxidation by Arrays of Molybdenum Doped Zinc Oxide Nanorods”, *ChemSusChem* 7 (2014) 2748.
8. T. Moon, L. Chen, S. Choi, C. Kim, and W. Lu, “Efficient Si Nanowire Array Transfer via Bi-Layer Structure Formation through Metal-Assisted Chemical Etching”, *Adv. Funct. Mater.* 13 (2014) 1949.
9. H. Chen, W. Li, H. Liu, and L. Zhu, “CdS Quantum Dots Sensitized Single- and Multi-Layer Porous ZnO Nanosheets for Quantum Dots-Sensitized Solar Cells”, *Electrochem. Comm.* 13 (2011) 331.
10. P. Sudhagar, T. Song, D. H. Lee, I. Mora-Seró, J. Bisquert, M. Laudenslager, W. M. Sigmund, W. I. Park, U. Paik, and Y. S. Kang, “High Open Circuit Voltage Quantum Dot Sensitized Solar Cells Manufactured with ZnO Nanowire Arrays and Si/ZnO Branched Hierarchical Structures”, *J. Phys. Chem. Lett.* 2 (2011) 1984.
11. C. Zhang, W. Tian, Z. Xu, X. Wang, J. Liu, S.-L. Li, D.-M. Tang, D. Liu, M. Liao, Y. Bando, and D. Golberg, “Photosensing Performance of Branched CdS/ZnO Heterostructures as Revealed by *in situ* TEM and Photodetector Tests”, *Nanoscale* 6 (2014) 8084.
12. B. Liu, Y. Sun, D. Wang, L. Wang, L. Zhang, X. Zhang, Y. Lin, and T. Xie, “Construction of a Branched ZnO-TiO₂ Nanorod Array Heterostructure for

Enhancing the Photovoltaic Properties in Quantum Dot-Sensitized Solar Cells”, *RSC Adv.* 4 (2014) 32773.

13. S. Zhu, L. Shan, X. Chen, L. He, J. Chen, M. Jiang, X. Xieab, and Z. Zhou, “Hierarchical ZnO Architectures Consisting of Nanorods and Nanosheets Prepared via a Solution Route for Photovoltaic Enhancement in Dye-Sensitized Solar Cells”, *RSC Adv.* 3 (2013) 2910.
14. H.-M. Cheng, W.-H. Chiu, C.-H. Lee, S.-Y. Tsai, and W.-F. Hsieh, “Formation of Branched ZnO Nanowires from Solvothermal Method and Dye-Sensitized Solar Cells Applications”, *J. Phys. Chem. C* 112 (2008) 16359.
15. S. H. Ko, D. Lee, H. W. Kang, K. H. Nam, J. Y. Yeo, S. J. Hong, C. P. Grigoropoulos, and H. J. Sung, “Nanoforest of Hydrothermally Grown Hierarchical ZnO Nanowires for a High Efficiency Dye-Sensitized Solar Cell”, *Nano Lett.* 11 (2011) 666.
16. C.-T. Wu, W.-P. Liao, and J.-J. Wu, “Three-Dimensional ZnO Nanodendrite/Nanoparticle Composite Solar Cells”, *J. Mater. Chem.* 21 (2011) 2871.
17. F. Zhao, X. Li, J.-G. Zheng, X. Yang, F. Zhao, K. S. Wong, J. Wang, W. Lin, M. Wu, and Q. Su, “ZnO Pine-Nanotree Array Grown from Facile Metal Chemical Corrosion and Oxidation”, *Chem. Mater.* 20 (2008) 1197.
18. V. González-Pedro, X. Xu, I. Mora-Seró, and J. Bisquert, “Modeling High-Efficiency Quantum Dot Sensitized Solar Cells,” *ACS Nano* 4, 5783 (2010).
19. H. Choi, C. Nahm, J. Kim, J. Moon, S. Nam, C. Kim, D.-R. Jung, and B. Park,

- “The Effect of TiCl₄-Treated TiO₂ Compact Layer on the Performance of Dye-Sensitized Solar Cell”, *Curr. Appl. Phys.* 12 (2012) 737.
- 20. C. Xu, P. Shin, L. Cao, and D. Gao, “Preferential Growth of Long ZnO Nanowire Array and Its Application in Dye-Sensitized Solar Cells”, *J. Phys. Chem. C* 114 (2010) 125.
 - 21. J. Kim, H. Choi, C. Nahm, C. Kim, S. Nahm, S. Kang, D.-R. Jung, J. I. Kim, J. Kang, and B. Park, “The Role of a TiCl₄ Treatment on the Performance of CdS Quantum-Dot-Sensitized Solar Cells”, *J. Power Source* 220 (2012) 108.
 - 22. H. Choi, J. Kim, C. Nahm, C. Kim, S. Nam, J. Kang, B. Lee, T. Hwang, S. Kang, D. J. Choi, Y.-H. Kim, and B. Park, “The Role of ZnO-Coating-Layer Thickness on the Recombination in CdS Quantum-Dot-Sensitized Solar Cells”, *Nano Energy* 2 (2013) 1218.
 - 23. J. Kim, H. Choi, C. Nahm, C. Kim, J. I. Kim, W. Lee, S. Kang, B. Lee, T. Hwang, H. H. Park, and B. Park, “Graded Bandgap Structure for PbS/CdS/ZnS Quantum-Dot-Sensitized Solar Cells with a Pb_xCdS_{1-x} Interlayer”, *Appl. Phys. Lett.* 102 (2013) 183901.
 - 24. J. Kim, H. Choi, C. Nahm, J. Moon, C. Kim, S. Nam, D.-R. Jung, and B. Park, “The Effect of a Blocking Layer on the Photovoltaic Performance in CdS Quantum-Dot-Sensitized Solar Cells”, *J. Power Sources* 196 (2011) 10526.
 - 25. H. Choi, T. Hwang, S. Lee, S. Nam, J. Kang, B. Lee, and B. Park, “The Construction of Tandem Dye-Sensitized Solar Cells from Chemically-Driven Nanoporous Photoelectrodes”, *J. Power Sources* 274 (2015) 937.

26. L. Green, M. Law, J. Goldberger, F. Kim, J. C. Johnson, Y. F. Zhang, R. J. Saykally, and P. D. Yang, “Low-Temperature Wafer-Scale Production of ZnO Nanowire Arrays”, *Angew. Chem. Int. Ed.* 42 (2003) 3031.
27. Y. Qiu, K. Yan, H. Deng, and S. Yang, “Secondary Branching and Nitrogen Doping of ZnO Nanotetrapots: Building a Highly Active Network for Photoelectrochemical Water Splitting”, *Nano Lett.* 12 (2012) 407.
28. Y. Zhao, H. Guo, H. Hua, and C. Hu, “Effect of Architectures Assembled by One Dimensional ZnO Nanostructures on Performance of CdS Quantum Dot-Sensitized Solar Cells”, *Electrochim. Acta* 115 (2014) 487.
29. W.-Q. Wu, H.-S. Rao, H.-L. Feng, H.-Y. Chen, D.-B. Kuang, and C.-Y. Su, “A Family of Vertically Aligned Nanowires with Smooth, Hierarchical and Hyperbranched Architectures for Efficient Energy Conversion”, *Nano Energy* 9 (2014) 15.
30. C. Nahm, H. Choi, J. Kim, D.-R. Jung, C. Kim, J. Moon, B. Lee, and B. Park, “The Effects of 100 nm-Diameter Au Nanoparticles on Dye-Sensitized Solar Cells”, *Appl. Phys. Lett.* 99 (2011) 253107.
31. W. Jia, B. Jia, F. Qu, and X. Wu, “Toward a Highly Efficient Simulated Sunlight Driven Photocatalyst: A Case of Heterostructured ZnO/ZnS Hybrid Structure”, *Dalton T.* 42 (2013) 14178.
32. Y. Yu, W. Ouyang, Z. Liao, B. Du, and W. Zhang, “Construction of ZnO/ZnS/CdS/CuInS₂ Core-Shell Nanowire Arrays via Ion Exchange: *p-n* Junction Photoanode with Enhanced Photoelectrochemical Activity under

Visible Light”, *ACS Appl. Mater. Inter.* 6 (2014) 8467.

33. P. Chhetri, K. K. Barakoti, and M. A. Alpuche-Aviles, “Control of Carrier Recombination on ZnO Nanowires Photoelectrochemistry”, *J. Phys. Chem. C* 119 (2015) 1506.
34. T. Olson, A. Chernov, B. Drabek, J. Satcher, and T. Han, “Experimental Validation of the Geometrical Selection Model for Hydrothermally Grown Zinc Oxide Nanowire Arrays”, *Chem. Mater.* 25 (2013) 1363.
35. L. Xu, Q. Chen, and D. Xu, “Hierarchical ZnO Nanostructures Obtained by Electrodeposition”, *J. Phys. Chem. C* 111 (2007) 11560.
36. C.-J. Chang, M.-H. Hsu, Y.-C. Weng, C.-Y. Tsay, and C.-K. Lin, “Hierarchical ZnO Nanorod-Array Films with Enhanced Photocatalytic Performance”, *Thin Solid Films* 528 (2013) 167.
37. Y. Lee, M. Stefik, L.-P. Heiniger, P. Gao, S. Seok, M. Gratzel, and M. K. Nazeeruddin, “Power from the Sun: Perovskite Solar Cells”, *Proceeding of the IEEE 40th Photovoltaic Specialist Conference, CO, Denver*, 2014, pp. 0943 – 0948.
38. B. Panigraphy, M. Aslam, D. S. Misra, M. Ghosh, and D. Bahadur, “Defect-Related Emissions and Magnetization Properties of ZnO Nanorods”, *Adv. Funct. Mater.* 20 (2010) 1161.
39. S. K. Chaudhuri, M. Ghosh, D. Das, and A. K. Raychaudhuri, “Probing Defects in Chemically Synthesized ZnO Nanostructures by Positron Annihilation and Photoluminescence Spectroscopy”, *J. Appl. Phys.* 108 (2010) 064319.

40. M. Gratzel, “Solar Energy Conversion by Dye-Sensitized Photovoltaic Cells”, *Inorg. Chem.* 44 (2005) 6841.
41. A. Zaban, M. Greenshtein, and J. Bisquert, “Determination of the Electron Lifetime in Nanocrystalline Dye Solar Cells by Open-Circuit Voltage Decay Measurements”, *ChemPhysChem* 4 (2003) 859.
42. B. Lee, J. I. Kim, S. Lee, T. Hwang, S. Nam, H. Choi, K. Kim, J. Kim, and B. Park, “Oriented Hierarchical Porous TiO₂ Nanowires on Ti Substrate: Evolution of Nanostructures for Dye-Sensitized Solar Cells”, *Electrochim. Acta* 145 (2014) 231.
43. C. Kim, J. Kim, H. Choi, C. Nahm, S. Kang, S. Lee, B. Lee, and B. Park, The “Effects of TiO₂-Coating Layer on the Performance in Nanoporous ZnO-Based Dye-Sensitized Solar Cells”, *J. Power Sources* 232 (2013) 159.
44. E. Guillen, E. Azaceta, A. Vega-Poot, J. Idigoras, J. Echeberria, J. A. Anta, and R. Tena-Zaera, “ZnO/ZnO Core-Shell Nanowire Array Electrodes: Blocking of Recombination and Impressive Enhancement of Photovoltage in Dye-Sensitized Solar Cells”, *J. Phys. Chem. C* 26 (2013) 117.
45. J. Tian, Q. Zhang, L. Zhang, R. Gao, L. Shen, S. Zhang, X. Qu, and G. Cao, “ZnO/TiO₂ Nanocable Structured Photoelectrodes for CdS/CdSe Quantum Dot Co-Sensitized Solar Cells”, *Nanoscale* 5 (2013) 936.

Appendix 2. List of Publications and Presentations

A.3.1. Publications (International):

1. **Woojin Lee**, Suji Kang, Taehyun Hwang, Kunsu Kim, Hyungsub Woo, Byungho Lee, Jaewon Kim, Jinhyun Kim, and Byungwoo Park,* "Facile Conversion Synthesis of Densely-Formed Branched ZnO-Nanowire Arrays for Quantum-Dot-Sensitized Solar Cells," *Electrochim. Acta* **167**, 194 (2015).
2. **Woojin Lee**, Taehyun Hwang, Sangheon Lee, Seung-Yoon Lee, Joonhyeon Kang, Byungho Lee, Jinhyun Kim, Taeho Moon,* and Byungwoo Park,* "Organic-Acid Texturing of Transparent Electrodes Toward Broadband Light Trapping in Thin-Film Solar Cells," *Nano Energy* (under revision).
3. **Woojin Lee**, Sungjin Shin, Dae-Ryong Jung, Jongmin Kim, Changwoo Nahm, Taeho Moon,* and Byungwoo Park* "Investigation of Electronic and Optical Properties in Al-Ga Codoped ZnO Thin Films," *Curr. Appl. Phys.* **12**, 628 (2012).
4. **Woojin Lee**,⁺ Hoechang Kim,⁺ Dae-Ryong Jung,⁺ Jongmin Kim, Changwoo Nahm, Junhee Lee, Suji Kang, Byungho Lee, and Byungwoo Park* "An Effective Oxidation Approach for Luminescence Enhancement in CdS Quantum Dots by H₂O₂" *Nanoscale. Res. Lett.* **7**, 672 (2012).
5. Yumin Kim,⁺ **Woojin Lee**,⁺ Dae-Ryong Jung, Jongmin Kim, Seunghoon Nam, Hoechang Kim, and Byungwoo Park,* "Optical and Electronic Properties of Post-Annealed ZnO:Al Thin Films," *Appl. Phys. Lett.* **96**, 171902 (2010).

6. Jae Ik Kim, **Woojin Lee**, Taehyun Hwang, Jongmin Kim, Seung-Yoon Lee, Suji Kang, Hongsik Choi, Saeromi Hong, Helen Hejin Park, Taeho Moon,* and Byungwoo Park,* "Quantitative Analyses of Damp-Heat-Induced Degradation in Transparent Conducting Oxides," *Sol. Energ. Mat. Sol. C.* **122**, 282 (2014)

7. Seung-Yoon Lee, **Woojin Lee**, Changwoo Nahm, Jongmin Kim, Sujin Byun, Taehyun Hwang, Byung-Gi Lee, Young Il Jang, Sungeun Lee, Heon-Min Lee and Byungwoo Park,* "Nanostructural Analysis of ZnO:Al Thin Films for Carrier-Transport Mechanisms," *Curr. Appl. Phys.* **13**, 775 (2013).

8. Seung-Yoon Lee, Taehyun Hwang, **Woojin Lee**, Sangheon Lee, Hongsik Choi, She-Won Ahn, Heon-Min Lee, and Byungwoo Park,* "Oxygen-Controlled Seed Layer in DC Sputter-Deposited ZnO:Al Substrate for Si Thin-Film Solar Cells," *IEEE J. Photovolt.* (2015).

9. Changwoo Nahm,⁺ Sungjin Shin,⁺ **Woojin Lee**, Jae Ik Kim, Dae-Ryong Jung, Jongmin Kim, Seunghoon Nam, Sujin Byun, and Byungwoo Park,* "Electronic Transport and Carrier Concentration in Conductive ZnO:Ga Thin Films," *Curr. Appl. Phys.* **13**, 415 (2013).

10. Chohui Kim, Hongsik Choi, Jae Ik Kim, Sangheon Lee, Jinhyun Kim, **Woojin Lee**, Taehyun Hwang, Suji Kang, Taeho Moon,* and Byungwoo Park,* "Improving Scattering Layer through Mixture of Nanoporous Spheres and Nanoparticles in ZnO-Based Dye-Sensitized Solar Cells," *Nanoscale Res. Lett.* **9**, 295 (2014).

A.3.2. Presentations (International):

1. **Woojin Lee**, Taehyun Hwang, Seung-Yoon Lee, Joonhyeon Kang, Taeho Moon, and Byungwoo Park, "Organic-Acid Texturing of Transparent Electrodes Toward Broadband Light Trapping in Thin-Film Solar Cells," *Materials Research Society (MRS) Spring Meeting*, San Francisco, CA, April 2015.
2. **Woojin Lee**, Taehyun Hwang, Seung-Yoon Lee, Joonhyeon Kang, Taeho Moon, and Byungwoo Park, "Organic-Acid Texturing of Transparent Electrodes Toward Broadband Light Trapping in Thin-Film Solar Cells," *International Conference on Electronic Materials and Nanotechnology for Green Environment (ENGE2014)*, Jeju, Korea, November 2014. [Oral by W. Lee]
3. **Woojin Lee**, Jae Ik Kim, Seung-Yoon Lee, Jongmin Kim, Joonhyeon Kang, Suji Kang, Taeho Moon, and Byungwoo Park, "Light Scattering Behavior of Highly Textured ZnO:Al Thin Films by Oxalic and Hydrochloric Acids," *Materials Research Society (MRS) Fall Meeting*, Boston, MA, November 2012.
4. **Woojin Lee**, Jae Ik Kim, Seung-Yoon Lee, Jongmin Kim, Joonhyeon Kang, Suji Kang, Taeho Moon, and Byungwoo Park, "Light Scattering Behavior of Highly Textured ZnO:Al Thin Films by Oxalic and Hydrochloric Acids," *Global Photovoltaic Conference 2012 (GPVC2012)*, Busan, Korea, November, 2012. [Poster by W. Lee]
5. Jae Ik Kim, **Woojin Lee**, Taehyun Hwang, Seung-Yoon Lee, Suji Kang, Hongsik Choi, Saeromi Hong, Taeho Moon, and Byungwoo Park, "Quantitative Understanding of Damp-Heat-Induced Degradation in

Transparent Conducting Oxides,"
Materials Research Society (MRS) Fall Meeting, Boston, MA, December 2013.

6. Byungwoo Park, Hongsik Choi, Jae Ik Kim, Seugnhoon Nam, **Woojin Lee**, Sungun Wi, Chohui Kim, and Joonhyeon Kang, "Nanoscale Interface Control for Photoluminescence and Solar-Cell Applications,"
The 9th Tsinghua University - University of Tokyo - Seoul National University Student Workshop, Seoul, Korea, October, 2013.
7. Jae Ik Kim, **Woojin Lee**, Jongmin Kim, Seung-Yoon Lee, Suji Kang, Taeho Moon, and Byungwoo Park, "The Stability and Degradation Mechanisms of ZnO:Al Thin Films in Damp-Heat Environment,"
Materials Research Society (MRS) Fall Meeting, Boston, MA, November 2012.
8. Jae Ik Kim, **Woojin Lee**, Jongmin Kim, Seung-Yoon Lee, Suji Kang, Taehyun Hwang, Taeho Moon, and Byungwoo Park, "The Stability and Degradation Mechanisms of ZnO:Al Thin Films in Damp-Heat Environment,"
The 13th Korea - Japan Student Symposium (Seoul National University - Tohoku University), Seoul, Korea, November, 2012.
9. **Woojin Lee**, Jae Ik Kim, Seung-Yoon Lee, Jongmin Kim, Joonhyeon Kang, Suji Kang, Taeho Moon, and Byungwoo Park, "Light Scattering Behavior of Highly Textured ZnO:Al Thin Films by Oxalic and Hydrochloric Acids,"
The 13th Korea - Japan Student Symposium (Seoul National University - Tohoku University), Seoul, Korea, November, 2012. **[Poster by W. Lee]**

10. **Woojin Lee**, Yumin Kim, Dae-Ryong Jung, Jongmin Kim, Seunghoon Nam, Hoechang Kim, and Byungwoo Park, "Optical and Electronic Properties of Post-Annealed ZnO:Al Thin Films," *International Conference on Electronic Materials and Nanotechnology for Green Environment (ENGE2010)*, Jeju, Korea, November 2010. [Oral by W. Lee]

11. **Woojin Lee**, Yumin Kim, Dae-Ryong Jung, Jongmin Kim, Seunghoon Nam, Hoechang Kim, and Byungwoo Park, "Optical and Electronic Properties of Post-Annealed ZnO:Al Thin Films," *The 11th Korea - Japan Student Symposium (Seoul National University - Tohoku University)*, Seoul, Korea, November, 2012. [Oral by W. Lee]

12. Sungjin Shin, **Woojin Lee**, Jongmin Kim, Dae-Ryong Jung, and Byungwoo Park, "Electronic and Structural Properties of Post-Annealed ZnO:Ga Thin Films," *The 11th Korea - Japan Student Symposium (Seoul National University - Tohoku University)*, Seoul, Korea, November, 2010.

A.3.3. Presentations (Domestic):

1. Byungwoo Park, Hongsik Choi, Jae Ik Kim, Seunghoon Nam, **Woojin Lee**, Sungun Wi, Chohui Kim, and Joonhyeon Kang, "Nanoscale Interface Control for Photoluminescence and Solar-Cell Applications," *秋季한국세라믹학회*, Jeju, Korea, October 16-18, 2013.

국문 초록

실리콘 박막 태양전지에 널리 사용되고 있는 아연산화물 기반 박막 투명 전극에 대하여, 유기산을 이용한 표면 식각 방법에 대한 연구를 진행하였다. 통계적 및 계산적 기법을 사용하여 식각된 표면 형상을 비교 분석하였고, 결정립 (grain) 과 결정립 경계 (grain boundary) 의 식각 속도 차이를 바탕으로 식각 메커니즘을 제안하여, 알루미늄 도핑된 아연산화물 투명 전극의 광대역 광포획 특성의 원인을 설명하였다. 본 박사학위 논문에서는 아연산화물 기반 투명전극박막의 식각 메커니즘을 기준의 연구 결과보다 체계적으로 설명하고 옥살산 (oxalic acid) 을 이용한 새로운 식각 기술을 제시하였고, 이를 통해 투명 전극 박막과 더 나아가 박막 태양전지의 광산란 특성 향상을 위한 기반을 마련했다는 점에서 그 학문적 의미를 찾을 수 있다.

주요어: 투명전극, 광 산란, 표면 텍스쳐링, 박막 태양전지, 아연 산화물

학번: 2011-31282